Australian Government
Bureau of Meteorology

The Centre for Australian Weather and Climate Research
A partnership between CSIRO and the Bureau of Meteorology

CSIRO

CAWCR Research Letters

Issue 8, August 2012

P. A. Sandery, T. Leeuwenburg, G. Wang, K. A. Day (editors)

www.cawcr.gov.au

ISSN: 1836-5949

Series: Research Letters (The Centre for Australian Weather and Climate Research); Issue 8.

Copyright and Disclaimer

Contents

Apparent and real sources of rainfall associated with a cutoff low in southeast Australia	Peter McIntosh, James Risbey, Jaclyn Brown and Michael Pook	4
SST forecast skill of the new intra-seasonal configuration of POAMA-2	Aurel Griesser and Claire Spillman	10
Characterizing westerly jets as objects	Lawrie Rikus, Gary Dietachmayer and Tracey Elliott	17
Oceansat-2 wind validation using OceanSITES moorings	Eric Schulz and Leon Majewski	20

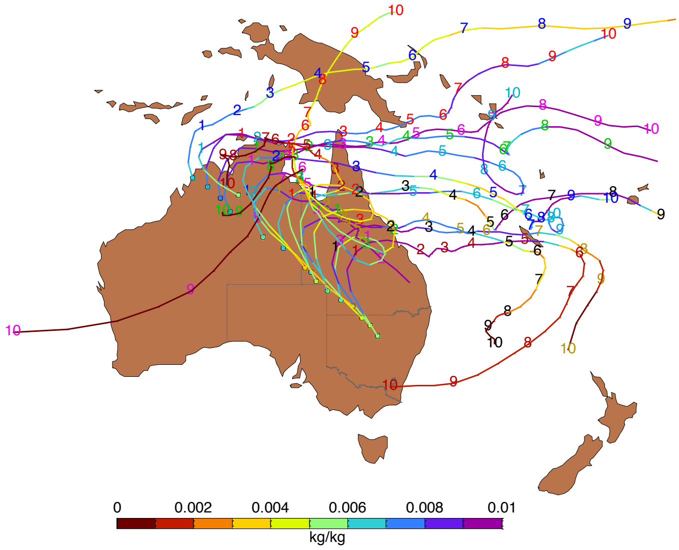

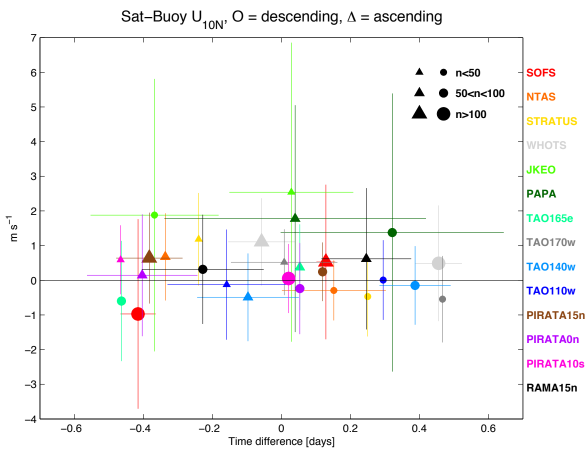

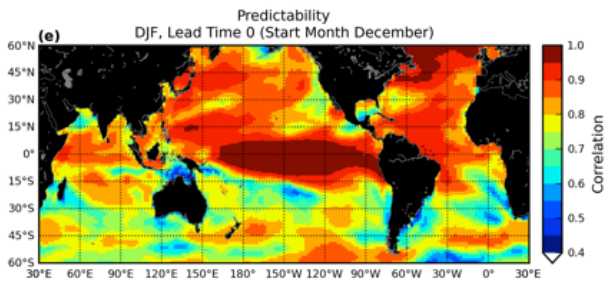

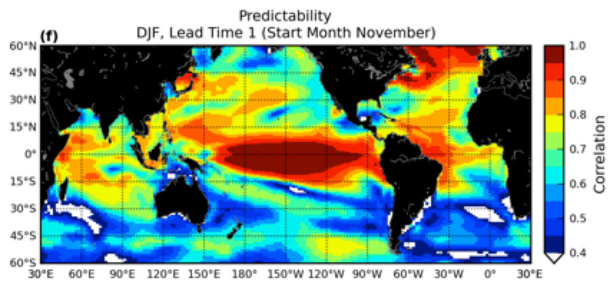

Editors: P.A. Sandery, T. Leeuwenburg, G. Wang, K.A. Day
Enquiries: Dr Paul Sandery p.sandery@bom.gov.au
CAWCR Research Letters
The Centre for Australian Weather and Climate Research
Bureau of Meteorology
GPO Box 1298 Melbourne VICTORIA 3001

CAWCR Research Letters is an internal serial online publication aimed at communication of research carried out by CAWCR staff and their colleagues. It follows on from its predecessor *BMRC Research Letters.* Articles in *CAWCR Research Letters* are peer reviewed. For more information visit the *CAWCR* website.

Apparent and real sources of rainfall associated with a cutoff low in southeast Australia

Peter C. McIntosh, James S. Risbey, Jaclyn N. Brown and Michael J. Pook

The Centre for Australian Weather and Climate Research

CSIRO Climate Adaptation and Wealth from Oceans Flagships,

Hobart, Tasmania, Australia

peter.mcintosh@csiro.au

Introduction

April to October rainfall in southeast Australia is of fundamental importance to agriculture. In particular, dryland cropping of wheat and other grains depends almost entirely on this growing-season rainfall. It is essential to understand the rainfall mechanisms in this region, and hence the way rainfall might be affected by remote climate drivers such as El Niño Southern Oscillation and the Indian Ocean Dipole. Such an understanding could enhance our development and use of seasonal forecast models.

The synoptic weather systems associated with April to October rainfall in the Mallee/Wimmera region of southeast Australia have been identified (Pook et al. 2006). The most important systems for rainfall are cutoff lows and fronts, and these typically travel across (or just south of) much of the continent from west to east.

Anecdotal evidence from farmers, agronomists and agricultural researchers indicates a general belief that much of the rainfall in the cropping regions of southeast Australia comes from the west. This appears to be based on three factors:

1. The observed eastward movement of weather systems and the associated rainfall;
2. The appearance of northwest cloudbands in satellite pictures; and
3. The emerging importance of the Indian Ocean for rainfall in the southeast of Australia.

This article examines the movement and moisture source of a cutoff low bringing rainfall to southeast Australia in June 2008.

The path of the rainfall is shown to be quite distinct from the trajectory of moist air feeding the rainfall, a result that has implications for understanding the effect of remote climate drivers on rain systems.

This case study adds to previous work on moisture inflow into cutoff lows in southeast Australia by examining the time evolution of a cutoff low and the associated rainfall and moisture trajectories. McIntosh et al. (2007) showed that higher rainfall events tend to have air parcel trajectories coming more from the north and north-east than the west and north-west when averaged over many cutoff lows bringing rainfall to the Mallee/Wimmera region. Brown et al. (2009) explored rainfall variations in three key El Niño years and showed that 1997 was not as dry as the other years due to several cutoff low events that sourced moisture from the north-east.

Cutoff lows are responsible for about half the total rainfall in the growing season and almost all of the high-rainfall events that are so important to farmers (Pook et al. 2006). A cutoff low is a cold-cored cyclonic system that typically forms in the mid-troposphere where it is identified by a minimum in the height of the 500 hPa surface. A cutoff low is vertically coherent and often, but not always, extends to the surface where it appears as a minimum in mean sea level pressure. The name arises because these systems tend to become separated or cut-off from the mid-latitude westerlies to their south (unlike the embedded fronts). Despite this separation, the systems normally propagate slowly from west to east.

Another synoptic feature that has been identified as being potentially important to rainfall in southeast Australia is the northwest cloudband (Tapp and Barrell 1984; Wright 1997; Telcik and Pattiaratchi 2001). The cloudband can be seen clearly on satellite images extending from the Indian Ocean northwest of Australia down towards the southeast. It is tempting to assume that this cloudband indicates the path of moisture feeding rainfall in the southeast.

There are a number of large-scale remote drivers of rainfall in southeast Australia (Risbey et al. 2009; Nicholls 2010). One of these is the Indian Ocean Dipole (IOD), which has also been implicated in the recent long-term drought in this region (Ummenhofer et al. 2009a). The Indian Ocean might act as a moisture source for northwest cloudbands which originate from this region (e.g. Ummenhofer et al. 2009a), albeit somewhat south of the equatorial region defining the IOD (Saji et al. 1999). Alternatively, ocean temperature gradients may alter the atmospheric dynamics by modifying the thermal wind (Ummenhofer et al. 2009b).

The eastward movement of cutoff lows, the appearance of northwest cloudbands, and the importance of the IOD for rainfall in the southeast of Australia would all seem to imply that a key source of moisture for rainfall in the southeast might be the Indian Ocean. We use a case study of a cutoff low in June 2008 to demonstrate that while rainfall may appear to come from the west, it is possible for the moisture source to actually be to the northeast.

Data and Methods

Gridded Australian daily rainfall comes from the SILO dataset (Jeffrey et al. 2001), which is based on spatial interpolation of high-quality station rainfall observations. All other data are obtained from the optimal model/data re-analysis produced by the National Centers for Environmental Prediction (NCEP) - National Center for Atmospheric Research (NCAR) (NCEP re-analysis) (Kistler et al. 2001). The NCEP reanalysis provides, amongst other variables, three-dimensional velocity, temperature and humidity on a global grid. The horizontal grid spacing is 2.5 degrees of longitude and latitude, the vertical spacing is variable but of order 100 hPa in the troposphere, and the temporal spacing is six hours.

One of the ways to explore the source of moisture to synoptic systems such as cutoff lows is to trace the origin of air parcels that end up over the Mallee/Wimmera region on wet days (McIntosh et al. 2007; Brown et al. 2009). Rain is typically produced from clouds in the lower-middle atmosphere, say around 700 hPa. By backtracking air parcels from this altitude above a number of rainfall stations in the region we gain an understanding of the origin and coherence of air parcel trajectories associated with rainfall events. By examining the specific humidity along the tracks, we can infer where moisture is entrained as well as where it is lost as rainfall.

Air parcel trajectories are obtained by solving the kinematic differential equation

$$\frac{D\mathbf{x}}{Dt} = \mathbf{v} \qquad (1)$$

where D/Dt is the substantial derivative following the flow, $\boldsymbol{x}$ is the unknown three-dimensional position (x,y,p) of an air parcel, and $\boldsymbol{v}$ is the specified three-dimensional velocity (u,v,ω), with ω being vertical velocity in pressure coordinates. The equation is solved backwards in time starting at the location of one or more rainfall stations in the Mallee/Wimmera. Once the air parcel trajectory is calculated, specific humidity is interpolated from gridded values onto the trajectory.

The trajectory equation (1) is solved using a semi-Lagrangian algorithm to ensure numerical stability given the lack of fine-resolution data in time (Staniforth and Cote 1991). The basic algorithm is:

1. Linearly interpolate velocity to the starting point;
2. Use this velocity to take an Euler step backwards for half a time step, giving an estimate of the mid-point of the trajectory for this time step;
3. Use cubic spline interpolation to find the velocity at the mid-point;
4. Iterate steps 2 and 3 to find a better estimate of the mid-point position and velocity (we use three iterations);
5. Use the mid-point velocity to take a step backwards the entire time step of six hours.

In this study we used the method to calculate air parcel trajectories for a maximum of 10 days backwards in time. We tested the algorithm by specifying a circular, stationary, two-dimensional flow field with a radius of five degrees, similar to that of a typical pressure system in the Australian region. The velocity at this radius was 15 m/s. The exact solution is a circular trajectory of radius five degrees and a period of 58 hours (nearly 10 time steps of six hours). The algorithm was capable of tracking an air parcel around the pressure system with no discernible change in radius, and with an error in time of two hours. This equates to a spatial error of less than 4% of the distance travelled, which compares favourably to the difference between different trajectory models over a similar time period (Stohl et al. 2001).

We also tested the method on real data by calculating sets of trajectories defined in different ways and observing the spread. The sets were defined by:

1. Using eight key rainfall stations in the Mallee/Wimmera region (Pook et al. 2006) as starting points from a pressure of 700 hPa;
2. Using a central rainfall station (Birchip, 142.85°E, 35.97°S) and varying the starting pressure over the standard NCEP pressures 400, 500, 600, 700, 850 and 925 hPa;
3. Using a central rainfall station (Birchip) from 700 hPa and varying initial times by ±6 and ±12 hours from the central time;
4. Adding a normally-distributed random walk to the air parcel location at the end of each six hour step. The three-dimensional displacement had a standard deviation of 20% of the distance travelled by the air parcel in that time step. This was repeated over 50 realizations.

The sensitivity tests were repeated over many dates from 1956 to the present. The results were examined by eye on a case-by-case basis to determine if the spread seemed reasonable given the synoptic situation. In most cases, the spread was relatively small even after 10 days, with the majority of air parcel trajectories originating within 10 degrees of each other.

As a final test, air parcel trajectories were compared to those calculated using the HYSPLIT Lagrangian trajectory model of Draxler and Hess (1998). The present method is higher order than that used by HYSPLIT, a choice we found necessary in order to obtain acceptable accuracy for the circular test path. HYSPLIT contains many options for determining the vertical velocity field, including simply using the analysis field. When used in this mode, HYSPLIT produced similar trajectories to those of our method for the case study.

As a result of the testing we have considerable confidence that the air parcel trajectories give us a very good qualitative idea of the history of air parcels that are associated with rainfall events in the Mallee/Wimmera. Furthermore, we are confident that a single air parcel trajectory is generally representative of the local picture.

Results

In early June 2008, a moderate rainfall event occurred in the Mallee/Wimmera region of SE Australia. This region has been intensively studied by Pook et al. (2006) to determine the synoptic causes of rainfall based on eight high-quality rainfall stations in the region (shown in red in the first panel of Figure 1). Australian daily rainfall is measured to 0900 EST (Eastern Standard Time, 10 hours ahead of GMT), equivalent to 2300 UTC on the previous day. Hence the rainfall measuring period coincides approximately with calendar days in GMT. This particular rainfall event produced 11 mm in the 24 hours to 2300 UTC 9 June 2008, averaged across the eight stations. The rainfall was associated with a cutoff low, a synoptic system which has been determined to be responsible for about half the rainfall in the Apr-Oct period in this region (Pook et al. 2006). The amount of rainfall itself was not unusual, being about one third of the monthly average. What was striking about this event was the coherent and propagating spatial pattern of rainfall over the previous three days.

The Australia-wide daily rainfall for the three days up to and including the rainfall event shows a clear south-eastward propagation (Figure 1a). On 6 June, the rainfall is a maximum in the far north of Western Australia. Over the next three days the rain patch moves to the southeast until it reaches the southeast of the continent on 9 June. The rainfall in the Mallee/Wimmera region (shown in red in the first panel of Figure 1) is south of the rainfall maximum, but is nevertheless part of the same synoptic event. It would be very tempting to assert that the source of moisture for the rainfall in the Mallee/Wimmera region had its origins to the northwest, possibly from as far as the Indian Ocean. However, the real picture is more complicated, as will be revealed by synoptic analysis and by backtracking air parcels to find their source.

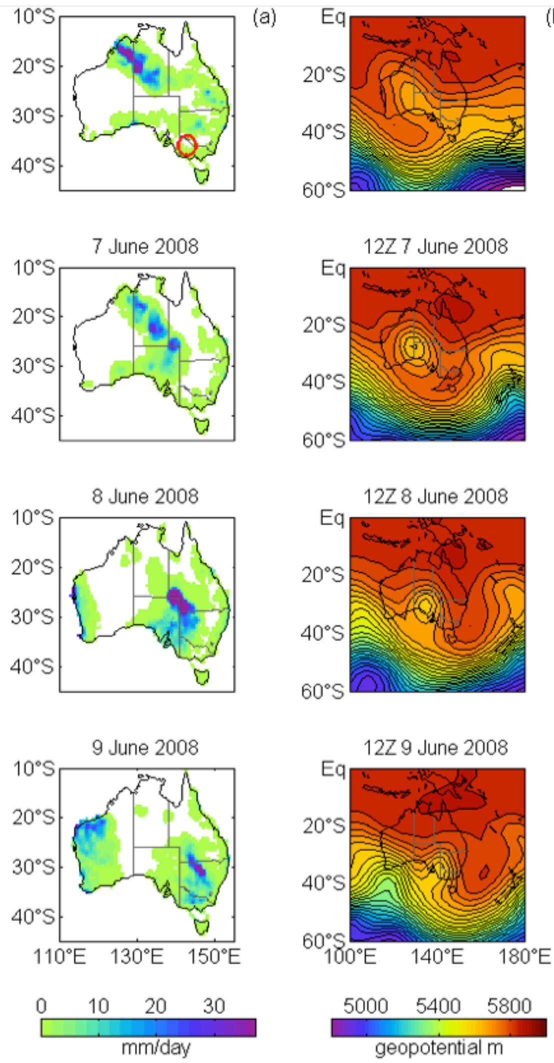

Figure 1: *(a) Daily rainfall in mm (24 hours to 2300 UTC). The Mallee/Wimmera region is indicated in red on the first diagram; (b) 500 hPa height contours at a time corresponding to the approximate mid-point of the rainfall period. Units are geopotential meters above sea-level.*

The synoptic situation, as indicated by the 500 hPa height contours (Figure 1b), shows a cutoff low moving westward and slightly southward. The north-east quadrant of a cutoff low is the region most likely to generate rainfall, and in our case study it is the region of maximum rainfall (compare Figures 1a and 1b). Air parcel trajectories are computed for the 10 days leading up to the rainfall event in the Mallee/Wimmera (Figure 2). We estimate that most of the rainfall occurred early on 9 June, based on examining changes in humidity in the NCEP data. Therefore, we choose the final trajectory time to be seven hours into the rainfall day, as this coincides with the standard NCEP reanalysis time of 0600 UTC 9 June 2008. The air parcel trajectories are not much different if this final time is varied by six hours either way.

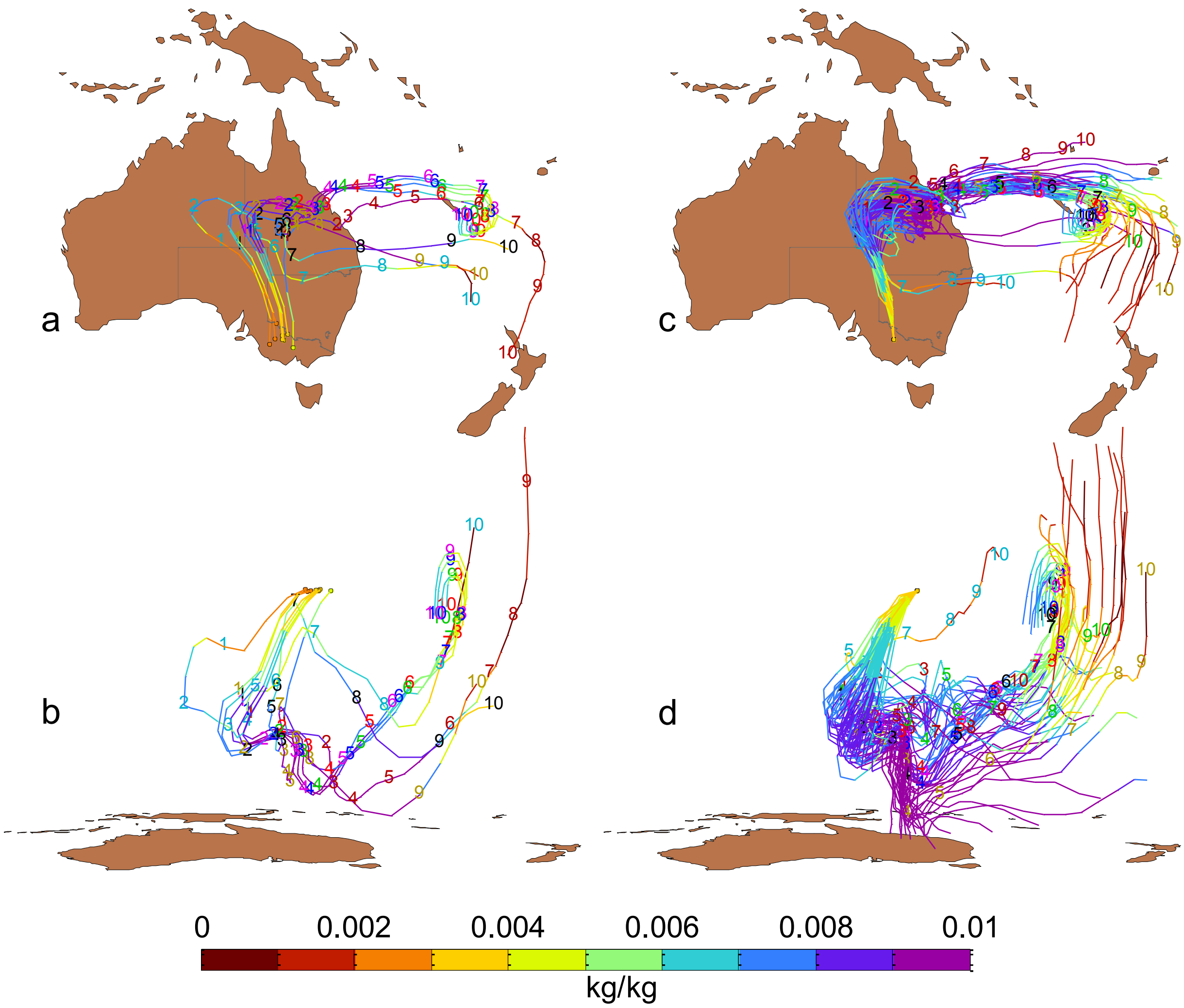

Figure 2: *Air parcel trajectories finishing over south-east Australia at 700 hPa at 0600 UTC 9 June 2008. The number of days prior to this time is indicated along the trajectories. The final time is indicated by coloured dots. Colours along the trajectories indicate specific humidity, with red being dry and purple wet. (a, b) Trajectories finishing at the eight rainfall stations in the Mallee/Wimmera region. (c, d) Ensemble of 50 trajectories finishing at the central station (Birchip) with 20% random noise added at each six hour step. The vertical axis in (b) and (d) is linear in pressure, and all trajectories end at 700hPa.*

The final height of the air parcel trajectories is chosen to be 700 hPa, which is an estimate of the height of the lower-middle level cloud layer that might be expected to produce rain at these latitudes. The NCEP humidity data confirms that this is a good choice for this rainfall event

The air parcel trajectories leading into the eight rainfall stations in the Mallee/Wimmera region are shown in plan view in Figure 2a and the vertical structure is shown in Figure 2b. The tracks are coloured according to the local specific humidity, with red indicating dry air and purple indicating wet air. To assess the sensitivity of trajectories to error sources such as lack of temporal and spatial detail and diffusive processes, 50 trajectories leading into the central station (Birchip) are calculated adding random noise as described in the methods section (Figures 2c and 2d).

Both sets of trajectories indicate that the air parcels carrying the moisture for this rainfall event originate over the Tasman Sea east of Australia, not the Indian Ocean as might have been expected. The perspective diagrams show that in the 10 days prior to the rainfall event, high altitude dry air descended into the marine boundary layer off the east coast of Australia and became much wetter, presumably through diffusive processes. This moist air at low levels then travelled westward over the continent before turning south and entering the north-east quadrant of the cutoff low where it was lifted up over the Mallee/Wimmera region, causing a decrease in specific humidity and producing rainfall.

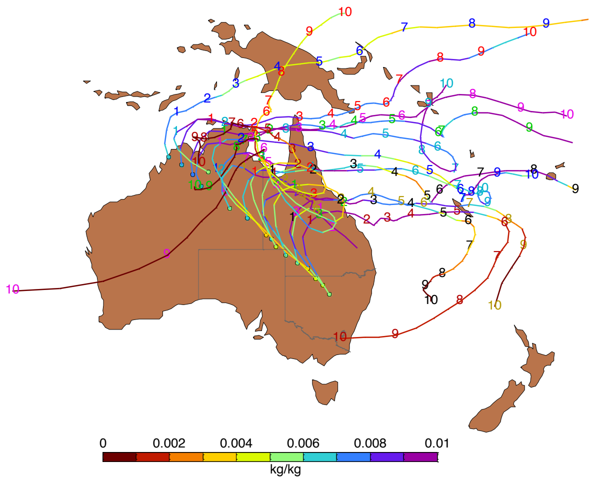

Figure 3: *Air parcel trajectories seeded at 1200 UTC on the four days 6-9 June 2008 along the path of maximum rainfall, and finishing at 700 hPa. The number of days prior to the seeding time is indicated along the trajectories. The color scale shows specific humidity along the trajectories.*

In the days prior to the rainfall event, the rain band appeared to travel south-eastwards towards the Mallee/Wimmera from the northwest of Australia (see Figure 1a). To explore the moisture inflow to this propagating rainfall event, we calculate air parcel trajectories along the path of maximum rainfall (see Figure 3). For simplicity, all trajectories finish at 1200 UTC on each day and terminate at 700 hPa. Although the picture is more confused than for the Mallee/Wimmera region, it does indicate that the rainfall event is being fed by moist air predominantly from the tropics to the northeast of the propagating cutoff low.

Discussion and Conclusion

The northwest to southeast progression of a rainfall event over the Australian continent in June 2008 is an ideal case study to explore the moisture source for an important synoptic situation associated with rainfall in southeast Australia. It is known that half the rainfall in this region in April-October is associated with synoptic systems known as cutoff lows (Pook et al. 2006), and the June 2008 rainfall event is of this type. It is tempting to assert that the moisture source for this rainfall in southeastern Australia is from the northwest, following the path of the rainfall event. However, backward air parcel trajectory analysis indicates that the moisture comes predominantly from the warm tropical waters to the north-east of Australia. The rainfall path itself simply indicates the progression of the cutoff low and particularly its north-eastern flank, which is the most effective sector at lifting air. In this sector the rainfall mechanism is characterized by upslide processes on isentropic surfaces, where warm, moist air originating over the tropics and sub-tropics is forced to rise as it moves southwards over colder air advected from the south by the cutoff low. This process is analogous to the 'warm conveyor belt' concept discussed by Wilson and Stern (1985). It is this warm, moist tropical air originating from the marine boundary layer that is lifted, cooled to saturation and subsequently makes the major contribution to the rainfall. By way of contrast, subsidence occurs predominantly on the western side of the cutoff.

The infrared and visible satellite images for this event (not shown) indicate the presence of a weak band of cloud propagating from the northwest to the southeast following the path of the cutoff low. It is unlikely that this band of cloud would qualify as a northwest cloudband (Telcik and Pattiaratchi 2001). A northwest cloudband generally appears as a coherent cloud extending from the northwest to the southeast of the continent simultaneously. The June 2008 event studied here is likely to be dynamically different from a northwest cloudband, but it does raise the possibility that the moisture source for a northwest cloudband could also be from the northeast rather than the northwest.

It should not be assumed that the moisture source for all rainfall associated with cutoff lows in south-eastern Australia is from the tropical oceans to the north-east. Brown et al. (2009) give examples of moisture pathways from cutoffs in different El Niño years, and show that while 1997 produced a number of wet events fed by moisture from the northeast, the cutoffs in 1982 and 2002 had drier trajectories from the west and southwest. This helps explain why 1997 was not unusually dry in south-eastern Australia despite the fact that El Niños generally cause dry conditions here, and 1997 was a very strong El Niño.

The results given here are consistent with a study of composites of air parcel trajectories over many cutoff low events in the same region (McIntosh et al. 2007). That work demonstrates that there is a tendency for higher rainfall events to have moisture sources from the north and north-east. Conversely, low rainfall events tend to have moisture pathways from the west and south-west.

The implications of this case study are important. There are an increasing number of studies of the effect of the Indian Ocean on rainfall in Australia (e.g. Nicholls 1989; Ashok et al. 2003; Ummenhofer et al. 2009a,b; Cai et al. 2009). It is becoming evident that the Indian Ocean may be as important as the Pacific Ocean in influencing rainfall over large parts of the country (Risbey et al. 2009). On the other hand, Brown et al. (2009) have shown the importance of trajectories originating over north-east Australia in generating Mallee/Wimmera rainfall in the 1997 El Niño event. Therefore it is important to understand the dynamical mechanisms by which ocean temperatures in the Indian Ocean are translated into rainfall over Australia. It is equally important to ensure that numerical models of the coupled ocean/atmosphere system represent these mechanisms accurately on weather forecasting, seasonal, decadal and longer timescales.

Acknowledgements

This work was supported in part by the Managing Climate Variability Program of the Grains Research and Development Corporation and by CSIRO's Climate Adaptation and Wealth from Oceans Flagships.

References

Ashok, K., Z. Guan and T. Yamagata, 2003: Influence of the Indian Ocean dipole on the Australian winter rainfall. *Geophys. Res. Lett.,* **30(15),** 1821, doi:10.1029/2003GL017926.

Brown, J.N., P.C. McIntosh, M.J. Pook and J.S. Risbey, 2009: An investigation of the links between ENSO flavors and rainfall processes in southeastern Australia. *Mon. Wea. Rev.,* **137,** 3786-3795, doi:10.1175/2009MWR3066.1.

Cai, W., T. Cowan and A. Sullivan, 2009: Recent unprecedented skewness towards positive Indian Ocean Dipole occurrences and its impact on Australian rainfall. *Geophys. Res. Lett.,* **36,** L19710, doi:10.1029/2009GL039902.

Draxler, R.R. and G.D. Hess, 1998: An overview of the HYSPLIT_4 modelling system for trajectories, dispersion and deposition. *Aust. Met. Mag.,* **47,** 295-308.

Jeffrey, S.J., J.O. Carter, K.B. Moodie and A.R. Beswick, 2001: Using spatial interpolation to construct a comprehensive archive of Australian climate data. *Environ. Modell. Software,* **16,** 309-330.

Kistler, R., E. Kalnay, W. Collins, S. Saha, G. White, J. Woollen, M. Chelliah, W. Ebisuzaki, M. Kanamitsu, V. Kousky, H. van den Dool, R. Jenne and M. Fiorino, 2001: The NCEP-NCAR 50-year reanalysis: Monthly means CD-ROM and documentation. *Bull. Amer. Meteor. Soc.,* **82,** 247-268.

McIntosh, P.C., M.J. Pook, J.S. Risbey, S.N. Lisson and M. Rebbeck, 2007: Seasonal climate forecasts for agriculture: Towards better understanding and value. *Field Crops Res.,* **104,** 130-138.

Nicholls, N., 1989: Sea surface temperature and Australian winter rainfall. *J. Climate,* **2,** 965-973.

Nicholls, N., 2010: Local and remote causes of the southern Australian autumn-winter rainfall decline, 1958-2007. *Climate Dyn.,* **34,** 835-845.

Pook, M.J., P.C. McIntosh and G.A. Meyers, 2006: The Synoptic Decomposition of Cool-Season Rainfall in the Southeastern Australian Cropping Region. *J. Appl. Meteorol. Climatol.,* **45,** 1156-1170.

Risbey, J.S., M.J. Pook, P.C. McIntosh, M.C. Wheeler and H.H. Hendon, 2009: On the remote drivers of rainfall variability in Australia. *Mon. Wea. Rev.,* **137,** 3233-3253.

Saji, N.H., B.N. Goswami, P.N. Vinayachandran and T. Yamagata, 1999: A dipole mode in the tropical Indian Ocean. *Nature,* **401,** 360-363.

Staniforth, A. and J. Cote, 1991: Semi-Lagrangian integration schemes for atmospheric models - a review. *Mon. Wea. Rev.,* **119,** 2206-2223.

Stohl, A., L. Haimberger, M.P. Scheele and H. Wernli, 2001: An intercomparison of results from three trajectory models. *Meteorol. Appl.,* **8,** 127-135.

Tapp, R.G. and S.L. Barrell, 1984: The northwest Australian cloud band: climatology, characteristics and factors associated with development. *J. Climate,* **4,** 411-424.

Telcik, N. and C. Pattiaratchi, 2001: The influence of northwest cloudbands on eastern Australian rainfall. Centre for Water Research Rep. UWA23, Univ. of Western Australia, Perth, Western Australia, Australia, 63 pp.

Ummenhofer, C.C, M.H. England, P.C. McIntosh, G.A. Meyers, M.J. Pook, J.S. Risbey, A. Sen Gupta and A.S. Taschetto, 2009a: What causes southeast Australia's worst droughts? *Geophys. Res. Lett.,* **36,** L04706, doi:10.1029/2008GL036801.

Ummenhofer, C.C, A. Sen Gupta, A.S. Taschetto and M.H. England, 2009b: Modulation of Australian precipitation by meridional gradients in east Indian Ocean sea surface temperature. *J. Climate,* **22,** 5597-5610.

Wilson, K.J. and H. Stern, 1985: The Australian summertime cool change. Part I: Synoptic and subsynoptic scale aspects. *Mon. Wea. Rev.,* **113,** 177-201.

Wright, W. J., 1997: Tropical-extratropical cloudbands and Australian rainfall: I. Climatology. *Int. J. Climatol.,* **17,** 807-829.

SST forecast skill of the new intra-seasonal configuration of POAMA-2

Aurel G. Griesser and Claire M. Spillman

Centre for Australian Weather and Climate Research

700 Collins St, Docklands, Victoria, 3008

A.Griesser@bom.gov.au

Introduction

The Australian Bureau of Meteorology's (the Bureau) seasonal prediction system Predictive Ocean and Atmosphere Model for Australia (POAMA) has been upgraded to version 2. The spatial skill of this model in predicting sea surface temperature (SST), as measured by the correlation of anomalies over the 29 year period 1982 to 2010, is documented herein.

POAMA is a dynamical global coupled model, and version 2 has been run operationally (fortnightly) since early 2011. POAMA exists in two configurations: a seasonal configuration which is run nine months into the future and is used for operational products, and an intra-seasonal configuration (also known as the multi-week configuration) which has been developed more recently and is (currently) run routinely in research mode to four months into the future. The intra-seasonal configuration is scheduled to replace the seasonal configuration operationally during 2012. Operational products currently utilising POAMA include seasonal ENSO outlooks (http://www.bom.gov.au/climate/enso/) and SST anomaly information for the Great Barrier Reef (Spillman 2011).

This study documents a baseline spatial SST skill assessment of POAMA version 2, and compares the skill of the intra-seasonal configuration with the skill of the existing seasonal configuration.

Method

POAMA consists of a coupled ocean-atmosphere climate model and data assimilation systems (Wang et al. 2008; Zhao and Hendon 2009; Lim et al. 2009; Hudson et al. 2011b).

The atmospheric component of POAMA 2 is the BoM unified atmospheric model (Colman et al. 2005), which has T47 horizontal resolution and 17 vertical levels. The ocean component is the Australian Community Ocean Model (ACOM) version 2 (Schiller et al. 1997). Resolution of the ocean model grid is 2° in the zonal direction; in the meridional direction, resolution is 0.5° near the equator, increasing to 1.5° near the poles. There are 25 vertical levels. The ocean-atmosphere coupler is OASIS: Ocean Atmosphere Sea Ice Soil system (Valcke et al. 2000).

POAMA exists in two configurations: seasonal and intra-seasonal. Both configurations utilise the same model components, though the data assimilation and initialisation schemes differ slightly (Table 1). For both configurations, three sub-model configurations exist, differing from each-other only in minor aspects of the implementation of certain physics (Lim et al. 2010, Hudson in prep.). Such a pseudo multi-model ensemble approach allows some model uncertainty to be captured and model errors to be reduced.

The seasonal configuration is initialised with a set of perturbed ocean states, but identical atmosphere and land initial conditions. Each of the three sub-models is run with ten ensembles, using the same set of ten perturbed ocean initial conditions. These perturbed ocean states are produced using POAMA Ensemble Ocean Data Assimilation System (PEODAS; Yin et al. 2011). The central PEODAS re-analysis forms the reference data used in this investigation. The atmosphere and land initial conditions are generated using the Atmosphere-Land Initialisation (ALI) scheme, by nudging the model's atmospheric state towards the observed state (either ERA-40 reanalyses, before Aug 2002, or the Bureau's operational numerical weather prediction models thereafter; Hudson et al. 2011b).

The lack of atmospheric perturbations has been found to result in insufficient ensemble spread in the first month (Hudson in prep.), which is acceptable on a seasonal timescale, but is not ideal for shorter (intra-seasonal) timeframes (Hudson et al. 2011b). Hence for the intra-seasonal configuration, a set of perturbed atmospheric initial conditions more in balance with the perturbed ocean states is produced using a coupled ocean-atmosphere ensemble initialisation system (Okely et al. 2011). The intra-seasonal configuration of POAMA initialises each of the three sub-models with one set of eleven perturbed coupled ocean-atmosphere-land initial states.

Marshall et al. (2011); Hudson et al. (2011b); Lim et al. (2010); and Hudson (in prep.) provide a complete description of the model and its systems. The seasonal and intra-seasonal configurations have different run schedules and forecast durations (the length of time into the future for which the forecast is produced; Table 1). For this study, retrospective forecasts (hindcasts) from the 1st day of each month were used.

Monthly-mean climatological SST was calculated for each calendar month and lead time at each grid point. Climatologies for PEODAS and the ensemble mean of each sub-model were calculated over the time period 1982 to 2010. The SST anomaly is the difference between the (predicted or observed) SST during a particular month and the climatological value for the month at that location (and lead time if for a forecast). SST anomalies were calculated first for each sub-model (using that sub-model's climatology), then averaged to produce model anomalies, while PEODAS SST anomalies were calculated using the PEODAS-derived climatology.

The skill of POAMA was assessed by correlating (Pearson's correlation) the model's SST anomalies with PEODAS SST anomalies for the period 1982 to 2010.

Table 1: *Principal differences between seasonal and intra-seasonal configurations of POAMA.*

	Seasonal Configuration	***Intra-Seasonal Configuration***
Sub-models	3	3
Initial Conditions	One set of 10 ocean states, identical atmospheric states	One set of 11 coupled ocean-atmosphere-land initial states
Total Ensemble Members	30	33
Initialised Dates (Operational)	1st & 15th of each month	1st, 11th and 21st of each month
Initialised Dates (Hindcast Mode)	1st day of each month	1st, 11th and 21st of each month
Forecast Duration	9 months	4 months

Standard deviation of the model was calculated as the average value of each individual ensemble member's standard deviation, rather than the standard deviation of the ensemble mean. This more accurately reflects the model's ability to simulate observed variability. Lead times are presented in months, with a lead time of zero corresponding to the month immediately following forecast initialisation. This study examined hindcasts initialised on the 1st day of each month, from both configurations of POAMA. To produce seasonal hindcasts, hindcasts initialised at one particular date are averaged over the lead time dimension for three months. For example, to produce the seasonal December-January-February (DJF) hindcast at lead time zero which is initialised on the 1st of December, SST anomalies for December at lead time 0, January at lead time 1, and February at lead time 2 were averaged.

Persistence forecasts were produced based on PEODAS reanalysis data. A persistence forecast is one baseline performance level, which involves minimum effort to produce, against which a forecasting model can be judged. The persistence forecast for the months of DJF at lead 0 persists the previous November's SST anomalies for the season, while for DJF at lead 1, the previous October's SST anomalies are used. June-July-August (JJA) persistence forecasts at lead times 0 and 1 used observed SST anomalies from the previous May and April respectively. The skill of the persistence forecast was assessed in the same way as the skill of the model forecast, allowing for direct comparison. A model predictability limit was estimated by means of a perfect model experiment. Each ensemble member was correlated with the mean of the remaining ensemble members within the sub-model. The average of all of the resulting correlations was taken to be the estimated predictability limit of the intra-seasonal model.

Results

Skill of persistence and POAMA hindcasts, and the estimated predictability limit are shown in Figure 1 for DJF at lead time zero and one month, calculated over the period 1982 to 2010. The model's skill is greatest (correlation above 0.9) over the central and eastern equatorial Pacific Ocean, and decreases considerably at lead time one (Figure 1c,d). Away from the tropics, there are areas of skill above 0.8 at lead time zero, particularly in the north Pacific ocean, though skill is generally lower. The persistence hindcast skill shown in Figure 1a,b is the level of skill, which the dynamical model must exceed in order to provide value. For SST anomalies over the period 1982-2010, POAMA shows greater skill than persistence over significant areas of the world's oceans, particularly over the maritime continent and the adjacent eastern Indian Ocean. The difference between POAMA's skill and that of persistence generally increases with lead-time. The estimated model predictability is highest, above 0.9, across the central and eastern equatorial Pacific (Figure 1e,f), a region in which both persistence and the dynamical model hindcasts also show skill above 0.9. In the southern Indian Ocean and the south Atlantic, POAMA's skill is up to 0.6 less than the model predictability limit.

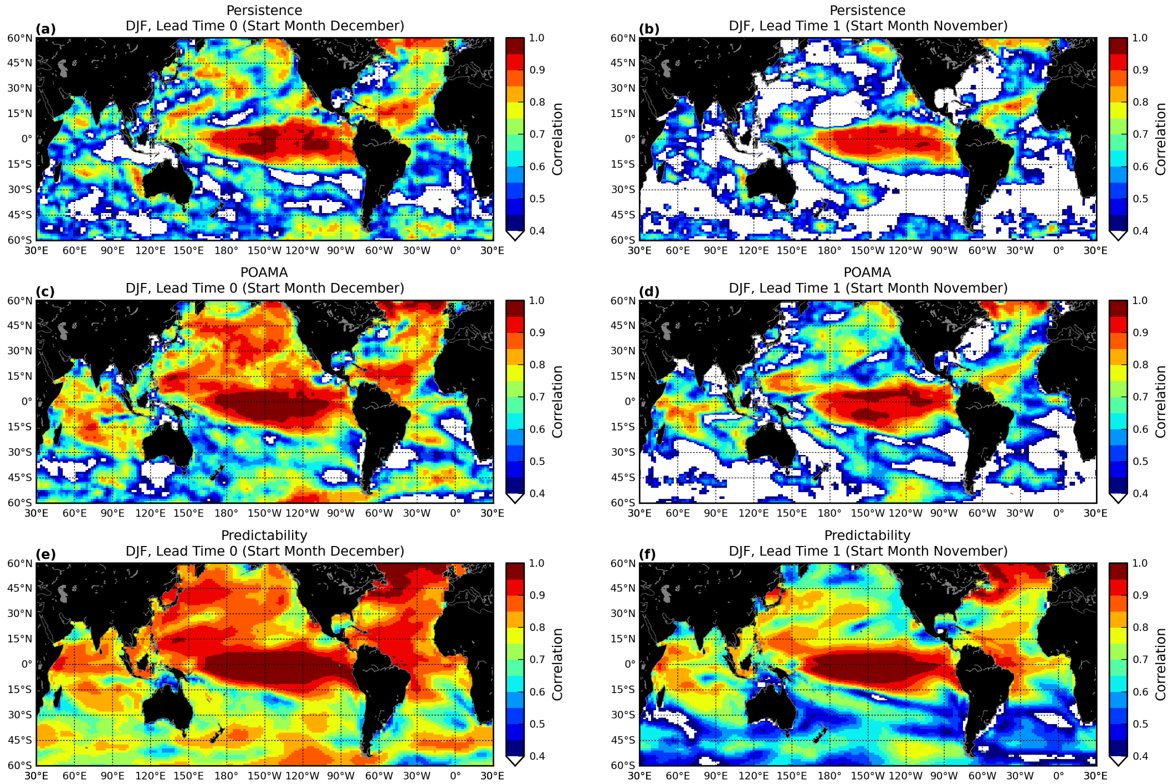

Figure 1: *Skill of persistence hindcasts at (a) lead time 0 and (b) lead time 1; skill of POAMA (intra-seasonal) hindcasts at (c) lead time zero 0 and (d) lead time 1; and estimated predictability limits at (e) lead time 0 and (f) at lead time 1, for DJF 1982 to 2010. Correlations below the statistically significant level are not shaded (0.37 for n=29 pairs of data).*

Figure 2 shows the same quantities as Figure 1, but for JJA. The highest model skill (correlation above 0.8) occurs over the tropical Pacific and the south Pacific Ocean, and (as for DJF) decreases considerably at lead time one (Figure 2c,d). In the northern Pacific and Atlantic Oceans skill is generally below 0.7. The persistence skill at lead time zero is above 0.8 in parts of the Pacific Ocean and Atlantic Ocean, though patchy overall (Figure 2a,b). At lead time one, persistence skill has reduced considerably, with only small patches above 0.8, and many areas no longer significantly correlated. As in DJF, POAMA is more skilful than persistence over large areas of the world's oceans, although in the tropical south Atlantic Ocean from 0°S to 15°S, persistence skill is up to 0.4 higher than POAMA's. Model predictability is heavily skewed towards the southern hemisphere (Figure 2e,f), with most of the southern hemisphere above 0.9 at lead time zero and over 0.7 at lead time one. At lead zero, over much of the equatorial and southern Pacific Ocean model skill approaches the predictability limit, while at lead time one POAMA's skill is close to the model predictability limit only in small patches, primarily in the tropical Pacific Ocean.

Standard deviation of POAMA SST forecasts is compared with that of observations for DJF and JJA for lead times zero and one, over the period 1982-2010 (Figure 3). Observed variability is greatest in the central and eastern equatorial Pacific (Figure 3a,b). In general, observed SST variability is reproduced well by POAMA (Figure 3c-f). Model SST generally has higher standard deviation than observed SST in the Southern Ocean during DJF, and over much of the northern Pacific Ocean during JJA. A notable deficiency in model SST variability exists along the coastlines of Peru and Ecuador during JJA (Figure 3d,f), and extends into the Pacific Ocean along the equator, where the standard deviation of the model is up to half a degree less than is observed. The skill of the intra-seasonal and seasonal configurations of POAMA are compared in Figure 4. On average, the intra-seasonal configuration of POAMA is more skillful than the seasonal configuration at both lead times for DJF and JJA, particularly over the Indian Ocean at lead zero during DJF (Figure 4a), and over the northern Pacific and Atlantic Oceans during JJA (Figure 4b,d). However, over the central and eastern equatorial Pacific Ocean, differences in correlation were generally below 0.1 for both seasons and lead times, except for JJA at lead one, where the seasonal model's skill is higher than the intra-seasonal model's skill by up to 0.3.

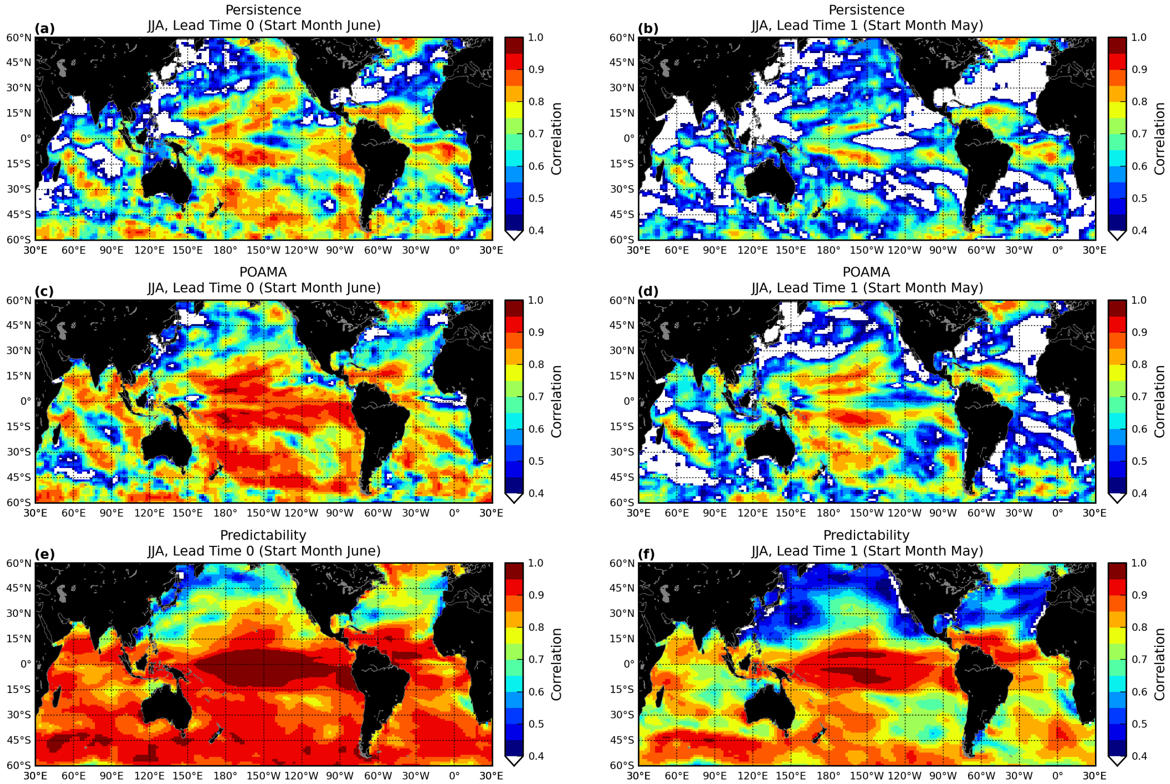

***Figure 2**: As Figure 1 but for JJA.*

Discussion

The intra-seasonal configuration of POAMA shows generally good skill for SST at lead times of zero and one month for DJF and JJA. In particular, over the equatorial Pacific Ocean correlation values are high, above 0.9, (a value of 1 corresponds to a perfect forecast), indicating that POAMA can forecast this region with good skill. POAMA's skill generally exceeds the skill of a persistence forecast, and approaches the model predictability limit.

Model skill is generally higher in the winter hemisphere (Figure 1 & Figure 2); in the northern hemisphere during DJF, and in the southern hemisphere during JJA. The higher model skill tends to correspond with areas of high persistence skill. The higher skill in the winter hemisphere is likely due in part to the deeper mixed layers (less density stratification) of surface waters which occur when there is less surface warming. The deeper mixed layer results in a more stable surface water temperature, which persists for longer and hence can generally be predicted with higher skill. As the eastern equatorial Pacific Ocean significantly influences global weather and climate (Trenberth 1997), a high degree of model skill in this area is important. Skill in this area can provide a level of predictability for various other climate parameters (such as rainfall) in many other parts of the world, provided that the model can reproduce the relevant teleconnections (McBride and Nicholls 1983; Sperber and Palmer 1996; Hudson et al. 2011a).

In the southern Indian Ocean and the south Atlantic, POAMA's skill is comparatively lower than in the Pacific Ocean, and degrades with lead time.

These areas appear to also present challenges in other seasonal dynamical general circulation models, as the Climate Forecast System from the National Centers for Environmental Prediction, and the System 3 model from the European Centre for Medium-Range Weather Forecasts also have difficulty in these regions (Wang et al. 2010; Stockdale et al. 2011). The general lack of skill in these regions is likely influenced by a relative scarcity of observations over much of the 1982-2010 verification period. In particular, sub-surface observations are limited prior to the launch of the ARGO program (Roemmich and Owens 2000; Clark et al. 2009) in 2000.

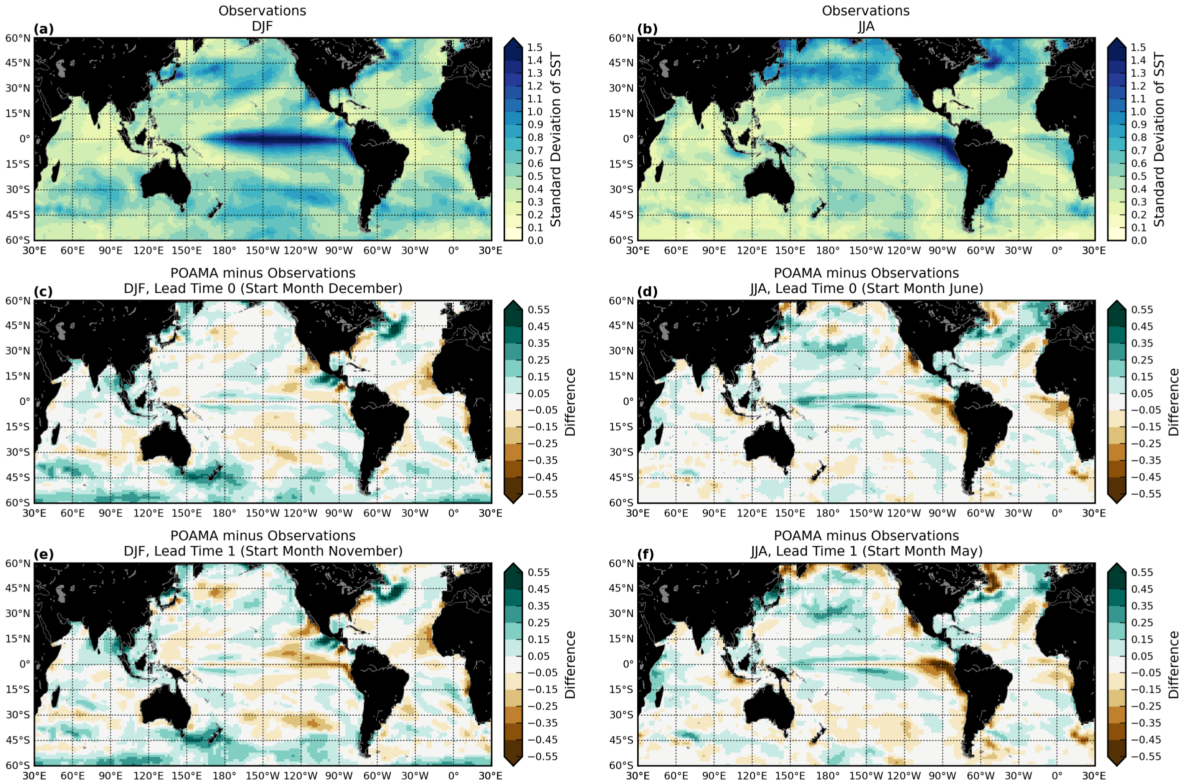

Figure 3*: Standard deviation of observed SST for (a) DJF and (b) JJA, and comparison with standard deviation of intra-seasonal model (model minus observations) for (c) DJF at lead 0, (d) JJA at lead 0, (e) DJF at lead 1 and (f) JJA at lead 1 for 1982-2010. Regions of green (brown) shading correspond to regions in which POAMA is more (less) variable than the forecast.*

There are limits to how accurate any forecast can be; the sources of forecast error can be broadly divided into two categories: errors arising due to uncertainty in the initial state, and model errors. Errors from the model include discretisation approximations and imperfect parameterisations. Uncertainty in the initial state is unavoidable, though as more observational systems are established, and measurement errors are reduced, the uncertainty can be expected to decrease (Alves et al. 2004).

Predictability estimates as calculated here neglect model error but give an indication of the effects of uncertainty in initial conditions on the forecast outcome. Where the model skill approaches predictability, further improvements in the observational system are likely to have positive impacts on skill. Conversely, where predictability is high but model skill is low, improvements in the observations are likely to be of relatively less benefit. In these areas, low skill is likely due to misrepresentation of physical behaviour (resulting from, for example, imperfect parameterisations, or errors from numerical discretisation), and better initial conditions will not result in a more accurate simulation

The actual predictability limit could be higher or lower than the estimated predictability calculated by the perfect model experiment. Model errors are unaccounted for, the real-world may have different predictability characteristics to the model, and there may be sources of real-world predictability which the model does not represent adequately. Additionally, the chaotic nature of turbulent fluid dynamical systems means that there will always be limits on the abilities of numerical models to predict the future of the ocean-atmosphere system. The seasonal configuration of POAMA is currently used operationally, but will be replaced by the intra-seasonal configuration in 2012. The intra-seasonal configuration's hindcasts will be extended to nine months duration. It is recommended that the skill comparison between the seasonal and intra-seasonal configurations (Figure 4) then also be extended. Other seasons could also be examined.

An aspect of POAMA in which there remains room for improvement is the level of skill in the Indian and Atlantic Ocean basins. Improved knowledge of relevant climate drivers and teleconnections may help in developing such skill. For some errors, post-processing calibration techniques may also result in more skilful forecasts, such as in the case of a feature being predicted in an incorrect location, or of consistently scalable amplitude.

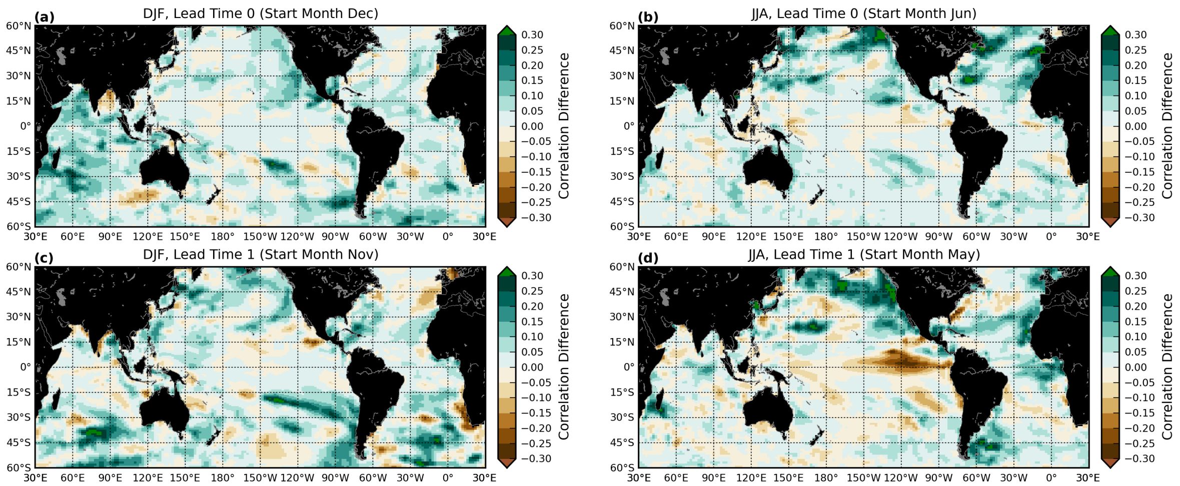

***Figure 4**: Differences between the skill of the intra-seasonal and seasonal configurations (intra-seasonal minus seasonal) for (a) DJF at lead 0, (b) JJA at lead 0, (c) DJF at lead 1, and (d) JJA at lead 1. Regions of green (brown) shading correspond to regions in which the intra-seasonal configuration is more (less) correlated with observations than the seasonal configuration.*

Acknowledgements

The authors would like to thank Goumin Wang, Faina Tseitkin and Griffith Young for the POAMA hindcasts, and Eun-Pa Lim and Guomin Wang for their thoughtful reviews.

References

Alves, O., M. A. Balmaseda, D. Anderson, and T. Stockdale, 2004: Sensitivity of dynamical seasonal forecasts to ocean initial conditions. *Quarterly Journal of the Royal Meteorological Society*, **130**, 647–667, doi:10.1256/qj.03.25.

Clark, C. et al., 2009: An Overview of Global Observing Systems Relevant to GODAE. *Oceanography*, **22**, 22-33, doi:10.5670/oceanog.2009.63.

Colman, R. et al., 2005: BMRC atmospheric model (BAM) version 3.0: comparison with mean climatology. *BMRC Research Report*, No. 106.

Hudson, D., O. Alves, H. H. Hendon, and A. G. Marshall, 2011a: Bridging the gap between weather and seasonal forecasting: intraseasonal forecasting for Australia. *Quarterly Journal of the Royal Meteorological Society*, **137**, 673–689, doi:10.1002/qj.769.

Hudson, D. A., O. Alves, H. H. Hendon, and G. Wang, 2011b: The impact of atmospheric initialisation on seasonal prediction of tropical Pacific SST. *Climate Dynamics*, **36**, 1155–1171, doi:10.1007/s00382-010-0763-9.

Lim, E.-P., H. H. Hendon, D. Hudson, G. Wang, and O. Alves, 2009: Dynamical Forecast of Inter–El Niño Variations of Tropical SST and Australian Spring Rainfall. *Monthly Weather Review*, **137**, 3796–3810, doi:10.1175/2009MWR2904.1.

Lim, E.-P., H. H. Hendon, O. Alves, Y. Yin, G. Wang, D. Hudson, M. Zhao, and L. Shi, 2010: Dynamical seasonal prediction of tropical Indo-Pacific SST and Australian rainfall with improved ocean initial conditions. *CAWCR Technical Report*, No. 032.

Marshall, A. G., D. A. Hudson, M. C. Wheeler, H. H. Hendon, and O. Alves, 2011: Evaluating key drivers of Australian intra-seasonal climate variability in POAMA-2: a progress report. *CAWCR Research Letters*, 10–16.

McBride, J. L., and N. Nicholls, 1983: Seasonal Relationships between Australian Rainfall and the Southern Oscillation. *Monthly Weather Review*, **111**, 1998–2004, doi:10.1175/1520-0493(1983)111<1998:SRBARA>2.0.CO;2.

Okely, P., O. Alves, D. A. Hudson, and Y. Yin, 2011: Towards coupled data assimilation: coupled covariance structures. *CAWCR Research Letters*, Issue

7, P.A. Sandery, T. Leeuwenburg, G. Wang, and K.A. Day, Eds.

Roemmich, D., and B. Owens, 2000: The Argo Project: Global Ocean Observations for Understanding and Prediction of Climate Variability. *Oceanography*, **13**, 45–50, doi:10.5670/oceanog.2000.33.

Schiller, A., J. S. Godfrey, P. C. McIntosh, and G. A. Meyers, 1997: A global ocean general circulation model for climate variability studies. *CSIRO Marine Laboratories Report*, No. 227.

Sperber, K. R., and T. N. Palmer, 1996: Interannual Tropical Rainfall Variability in General Circulation Model Simulations Associated with the Atmospheric Model Intercomparison Project. *Journal of Climate*, **9**, 2727–2750, doi:10.1175/1520-0442(1996)009<2727:ITRVIG>2.0.CO;2.

Spillman, C. M., 2011: Operational real-time seasonal forecasts for coral reef management. *Journal of Operational Oceanography*, **4**, 13–22.

Stockdale, T. N. and Coauthors, 2011: ECMWF seasonal forecast system 3 and its prediction of sea surface temperature. *Climate Dynamics*, **37**, 455–471, doi:10.1007/s00382-010-0947-3.

Trenberth, K. E., 1997: The Definition of El Niño. *Bulletin of the American Meteorological Society*, **78**, 2771–2777, doi:10.1175/1520-0477(1997)078<2771:TDOENO>2.0.CO;2.

Valcke, S., L. Terray, and A. Piacentini, 2000: Oasis 2.4, Ocean atmosphere sea ice soil: user's guide. Technical Report TR/CMGC/00/10, CERFACS, Toulouse, France.

Wang, G., O. Alves, D. Hudson, H. Hendon, G. Liu, and F. Tseitkin, 2008: SST skill assessment from the new POAMA-1.5 system. *BMRC Research Letters*, 8, 2–6.

Wang, W., M. Chen, and A. Kumar, 2010: An Assessment of the CFS Real-Time Seasonal Forecasts. *Weather and Forecasting*, **25**, 950–969, doi:10.1175/2010WAF2222345.1.

Yin, Y., O. Alves, and P. R. Oke, 2011: An Ensemble Ocean Data Assimilation System for Seasonal Prediction. *Monthly Weather Review*, **139**, 786–808, doi:10.1175/2010MWR3419.1.

Zhao, M., and H. H. Hendon, 2009: Representation and prediction of the Indian Ocean dipole in the POAMA seasonal forecast model. *Quarterly Journal of the Royal Meteorological Society*, **135**, 337–352, doi:10.1002/qj.370.

Characterizing westerly jets as objects

Lawrie Rikus, Gary Dietachmayer and Tracey Elliott

Centre for Australian Weather and Climate Research

700 Collins Street, Docklands, VICTORIA, 3008

l.rikus@bom.gov.au

Introduction

In assessing the performance of a climate model one of the fields which is traditionally examined is the zonal mean zonal wind *U* because the positions of the various jet streams show up as distinct areas of positive values. The position and shape of these regions provides information about the thermal structure of the model atmosphere and allows systematic errors in the simulations to be identified. In the past the evaluation of a model's performance in describing zonal mean *U* has been done qualitatively using subjective judgment or by calculating the overall root mean square (RMS) field difference with the corresponding climatological data.

The disadvantage of the former process is that it is time consuming, requires the evaluator to have reproducible skill and is difficult to automate. The disadvantage of the latter technique is that it is not sensitive to the detailed topology of the field and therefore is unable to give specific information about the individual jets. In this paper we describe an objective image processing-based approach that automatically identifies westerly jet-related blobs in the monthly zonal mean *U* field and captures their properties for further study. This objective identification of the regions as blobs facilitates the use of metrics based on position, size, shape and maximum and mean blob velocity. The time series of these properties can be used to produce climatologies and to tease out the influence of various climate drivers. The flexibility and efficiency of the process makes it ideal for routinely generating a number of metrics for climate model simulations and re-analysis products.

Defining westerly jet blobs

The fundamental feature of the zonal mean *U* field is the presence of local maxima with surrounding closed contours, which will hereafter be denoted as blobs. A number of ideas to define *U* blobs were trialed including one using a set of predefined thresholds but for consistency with the basic conceptual model of zonal wind jet structure the following algorithm was chosen. (For the application of blob identification techniques to other fields the choice of algorithm would depend on which blob properties were considered important such as area and orientation of closed contour areas for zonal temperature for example).

The jet blob algorithm is a series of steps that operate independently on each monthly mean zonal mean *U* field.

1. Identify all local maxima using a local mean field filter.
2. Sort the list of local maxima from largest to smallest to define the processing order for the following steps.
3. Characterise 'local' regions by defining a contour around each local maximum with value 1m/s less than the local maximum.
4. If there is no overlap with other local regions this is classified as a blob and its properties including the maximum and mean zonal mean U over the blob and the centre of mass coordinates are evaluated and tabulated.
5. Any blob requiring a threshold value of less than 10 m s^{-1} is discounted as being too small.

The choice of 1 m s^{-1} for the blob boundary and the minimum value of 10 m s^{-1} are essentially arbitrary but the overall properties of the time series of the blobs does not depend greatly on these choices. Smaller boundary thresholds do tend to capture more blobs but these tend to be marginal in terms of their isolation from other nearby structures. One consequence of these choices is that occasionally the local maximum velocity on one level is more than 1 m s^{-1} larger than the values at adjoining pressure levels resulting in the identification of 'line' blobs extended along a single pressure level. This is particularly a problem for stratospheric jets that intrude into the domain from the top levels. Line blobs are inconsistent with the concept of spatially extended jet-stream blobs and thus require an extra step to expand them by redefining the local region by decreasing the bordering contour value by 1 m s^{-1} successively until the defined blob either has a broader pressure structure or it overlaps another higher valued (and hence previously identified) blob and is subsumed into it.

The full algorithm was implemented as a small number of python scripts with the computationally complex aspects handled by standard scientific python image processing libraries (Jones et al, 2001) for efficiency; a 30 year time series of monthly means can be processed in less than 30 seconds on a desktop PC. This approach is very flexible and readily adaptable for other blob definition criteria.

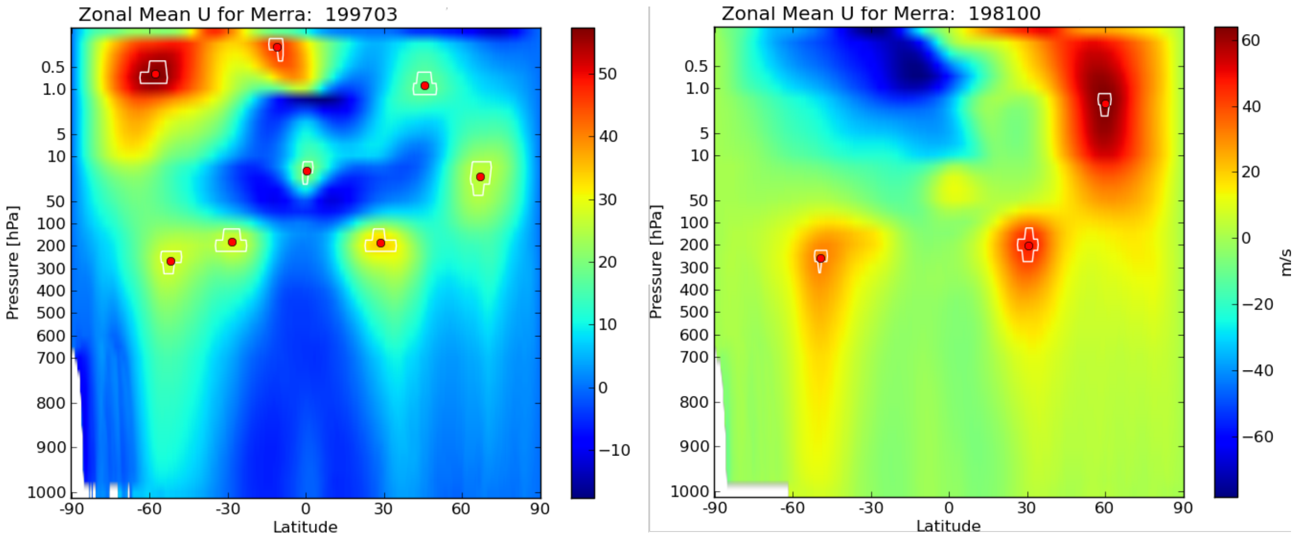

Figure 1: *Examples of blob identification for April 1997 (left) and January 1981 (right) for the Merra dataset. The blobs are identified by the red dots while the white contours surrounding them represent the defined blob extents. The colour intervals represent wind speed in m s^{-1} Note that the yellow 'blob' in the tropics at around 50 hPa in the right hand plot does not qualify because enclosing it requires a contour value below the arbitrary 10 m s^{-1} threshold.*

Results for the Merra Re-analysis

The Modern Era Reanalysis for Research and Applications (MERRA) (Rienecker et al, 2011) is a modern satellite era re-analysis produced by the NASA GSFC Global Modeling and Assimilation Office (GMAO) with a focus on the hydrological cycle. It was chosen for this study because it is available for pressure levels up to 0.1 hPa and is able to give a more complete representation of the stratospheric jet structures than the other re-analysis datasets. The data used here consisted of monthly mean zonal mean zonal wind *U* for the period January 1979 to December 2005. The blob analysis was run for each month in turn and all identified blobs recorded. There were just over 1600 blobs identified with an average of 5 per month. The monthly distribution of the number of blobs is shown in Figure 1.

The monthly number is largely determined by the fact that there is only one polar night jet and two subtropical jets in November to January and June to August. During the transition seasons the winter jet fades away while the corresponding stratospheric jet in the other hemisphere starts to establish itself. At the same time the summer subtropical jet weakens and the winter polar front jet develops so that there are often two connected centres, which are identified as two blobs. These seasonal number variations are augmented by the occurrence of 1-2 tropical stratospheric blobs. Two examples are shown in Figure 2, where the centroids of the identified blobs are marked by red spots and their defining contours are in white. Figure 3 shows the scatter of all the identified blobs in latitude-log (pressure) coordinates where the colour coding represents the month of occurrence (which allows a quick interpretation of the respective annual cycles), and the size of the circles is proportional to the maximum value of *U* for each blob. The different jet streams very clearly fall into readily identified groups with a distinct gap around the tropopause (around 100 hPa).

As expected the stratospheric winter jets have the largest magnitudes. The time evolution of the southern hemisphere polar night jet is obvious, starting at around 60 Pa in January, moving equatorward and upward in May-June and then descending and moving poleward towards the end of the year. The northern hemisphere equivalent is less well organised, although it does show a tendency to stay above 1 hPa during the last few months of the year with excursions down to higher pressure occurring mainly in the first half of the year.

In the tropics the blobs show a preference for the summer hemisphere suggesting a connection with the ITCZ. There is no obvious correlation of height with month of the year but the location suggests that the blobs are probably the westerly members of the jets associated with the QBO (Gabis and Troshichev, 2005).

In the troposphere it is difficult to separate the polar front and sub-tropical jets and there is a clear indication that (at least in a zonal sense) they behave as aspects of the same jet moving poleward in Autumn and equatorward in spring with little change in maximum wind. Histogram plots of latitude against month for the two tropospheric jets (not shown) show the southern tropospheric jet's transition to be very abrupt with the transition months often showing 2 separate blobs, while the northern jet shows a much smoother change over the year. This behaviour is consistent with the results of an investigation of the relationship between the subtropical and eddy-driven jets (Lee and Kim, 2003). There is also an isolated cluster of blobs closer to the north pole which may be connected to the polar front jet. Similar blobs appear in the south when the minimum threshold value of 10 m s^{-1} is reduced.

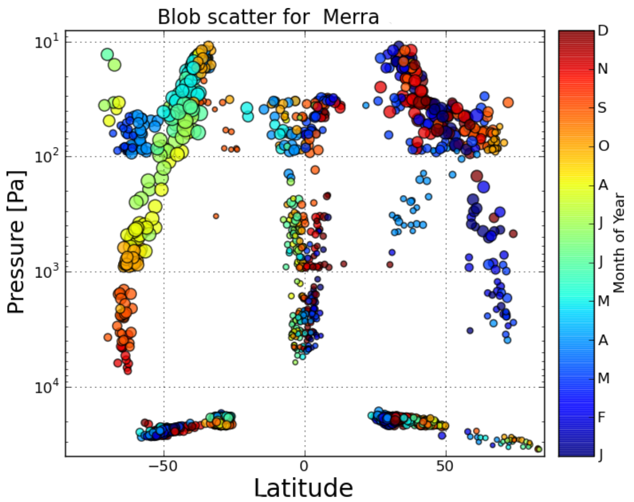

Figure 2: *Latitude-log (Pressure) scatter plot for all the blobs identified over the entire Merra time series. The colour gives the month of the year and the circle sizes are proportional to the maximum zonal windspeed of the blob.*

Conclusions

This paper has shown how using a flexible object identification approach can yield a rich harvest from a simple field like zonal mean zonal wind, producing a set of time series of blob properties corresponding to the well-known westerly wind jets.

This secondary information can be further processed by time series techniques etc to provide specific information about the jets and their temporal behaviour. The simplicity of the scheme introduced here means that it can be applied to re-analysis data as well as climate models to provide climatologies of jet properties that can be used as the basis of a set of jet-based model verification scores. The flexibility of the approach using python based tools means that it can also be readily applied to other fields. Although each new field will require different definitions for the relevant blob objects to ensure they encompass the required information, the framework can easily accommodate this.

Acknowledgements

The data used in this effort were acquired as part of the activities of NASA's Science Mission Directorate, and are archived and distributed by the Goddard Earth Sciences (GES) Data and Information Services Center (DISC).

References

Gabis, I., and Troshichev, O.A., 2005. QBO cycle identified by changes in height profile of the zonal winds: new regularities. J. Atmos. Sol. Terrestrial Phys., 67, 33-44, doi: 10.1016/j.jastp.2004.07.015

Jones, E., Oliphant, T., Petersen, P., et al, 2001, SciPy: Open Source Scientific Tools for Python, http://www.scipy.org/

Lee, S., and KimH.-K, 2003. The dynamical relationship between subtropical and eddy-driven jets, J. Atmos. Sci.,60, 1490-1503

Rienecker, M.M., M.J. Suarez, R. Gelaro, R. Todling, J. Bacmeister, E. Liu, M.G. Bosilovich, S.D. Schubert, L. Takacs, G.-K. Kim, S. Bloom, J. Chen, D. Collins, A. Conaty, A. da Silva, et al., 2011. MERRA - NASA's Modern-Era Retrospective Analysis for Research and Applications. *J. Climate*, 24, 3624-3648, doi: 10.1175/JCLI-D-11-00015.1.

Oceansat-2 wind validation using OceanSITES moorings

Eric W. Schulz and Leon Majewski

Centre for Australian Weather and Climate Research

700 Collins Street, Docklands, VICTORIA, 3008

E.Schulz@bom.gov.au

Introduction

Surface winds are an integral part of the dynamic atmosphere and interact with the underlying ocean. They are a tangible manifestation of many physical processes that occur in the atmosphere. The lower limbs of the Hadley circulation drive 'prevailing' winds in the lower latitudes; the "Roaring Forties" are one of the defining atmospheric characteristics of the Southern Ocean; while monsoon winds, "East Coast Lows", tropical cyclones and land-sea breezes are present across the spectrum of scales.

Observations of marine winds have been routinely collected for the last century primarily from ships (Kent et al. 2009), and more recently from drifting (Meldrum et al. 2009) and moored (McPhaden et al. 2009) buoy networks. Observations have underpinned growth in understanding of global atmospheric dynamics and lead to improvements in forecasting on daily, seasonal and climatic scales that impact on society.

The advent of satellite observations and the development of scatterometery (e.g. Stoffelen and Anderson 1997) over the past four decades has allowed for unprecedented access to routine observations of the ocean surface on a global scale (Lorenc 1986). This has greatly advanced our understanding of marine processes from Numerical Weather Prediction (NWP) of extreme events in traditionally data-sparse areas (Stoffelen et al. 1991, Atlas et al. 2001) and tropical cyclones (Leidner et al. 2003, Chen 2007), through to intra-seasonal (Madden et al. 2002, Senan et al. 2003, Fu 2003), monsoonal (Halpern 1998, Simon et al. 2006) and El Nino (Liu et al. 1998, Chen 1999) variability.

The feasibility of remotely measured surface marine winds from satellite borne microwave radars, known as scatterometers, was first established in 1973 and 1974 with the Skylab missions. This was followed by the 4-month Seasat satellite scatterometer mission in 1978 that demonstrated that accurate wind observations could be obtained from space. The European Space Agency's Remote Sensing Satellite-1 (ERS-1) mission in 1991 carried a single-swath scatterometer SCAT, and this was succeeded by ERS-2 in 1995. In late 1996 the NASA dual-swath *Ku*-band scatterometer NSCAT was carried by the ADEOS-Midori mission for 1 year and provided reliable marine wind observations. The early termination of NSCAT precipitated the launch of the SeaWinds scatterometer aboard the QuikSCAT mission in 1999, which was a resounding success and far outlived the design lifespan before failing in November 2009. The success of NSCAT and QuikSCAT in providing global coverage on a 2-day cycle was the motivation for launching another SeaWinds scatterometer on the ill-fated ADEOS-II satellite in 2002. The European Space Agency (ESA) ASCAT scatterometer (Figa-Saldaña et al. 2002) aboard the MetOp-A operational meteorology satellite became available in 2008.

The Australian Bureau of Meteorology commenced ingesting QuikSCAT (JPL 2001) satellite scatterometer winds into the operational NWP models in 2005 (NMOC 2006). Assimilation of ASCAT scatterometer data commenced in 2010 (NMOC 2010). Scatterometer data have also been used extensively to validate the marine wind (e.g. Buehner 2002, Leidner et al. 2003, Yuan 2004, Chelton and Freilich 2005, Kepert et al. 2005, Schulz et al. 2007) and wave model (Isaksen and Janssen 2004, Greenslade et al. 2005) forecasts provided by many national oceanographic and meteorological operational centres.

On the 23rd September 2009 ISRO launched PSLV-C14 carrying Oceansat-2, the second in a series of ocean research polar orbiting satellites (Padia 2010). The Oceansat-2 platform carries a *Ku*-band wind scatterometer (SCAT), the Ocean Colour Monitor (OCM), an imaging spectrometer, and a Radio Occultation Sounder for Atmospheric studies (ROSA). The main objectives of the Oceansat-2 mission are to provide continuity of the Oceansat-1 mission; provide retrieved geophysical parameters on an operational basis; and, to promote the application of these products to activities such as cyclone tracking, fisheries management and monitoring of coastal processes (Rao 2010). The importance of scatterometer winds derived from Oceansat-2 has increased due to the limited availability of operational scatterometers.

In 2010 the Bureau responded to ISRO's Oceansat-2 Announcement of Opportunity, gaining access to Oceansat-2 wind vectors in near real time. Here we provide a first look at verification of Oceansat-2 using independent in situ wind observations from a global network of moored buoys over a 1-year period.

Datasets

OceanSITES Moored Buoys

The Ocean Sustained Interdisciplinary Time-series Environment observation System (OceanSITES, Send et al. 2010) provides a framework for a unified network of high quality long-term moored buoy observations across the globe. The moorings collect wind and other meteorological and oceanographic measurements (e.g. Cronin et al. 2012). Observations are typically stored as 1-minute averages, but near-real-time data is averaged to hourly or daily values (depending on the operating organisation). Here we average all *in situ* data to daily averages. A 1-year period (17 March 2010 to 17 March 2011) is used for the validation period and has been selected to match the availability of the Southern Ocean Flux Station (SOFS) data (Schulz et al. 2012). Scatterometers observe the ocean surface roughness on the cm scale that relates directly to wind stress and indirectly to the wind – ocean surface velocity difference. Omitting the ocean current from bulk flux calculations may result in large errors (Kelly et al. 2001). Chelton et al. (2004) estimated errors as large as 1 m s^{-1} for regions with strong currents. The scatterometer observations are used to derive a wind that would exist at a standard height of 10 m if the atmospheric conditions were neutrally stable (U_{10N}). Wind observations are typically collected on the moorings at a height of 2-3 m above the water, and hence for direct comparison with scatterometer observations must be corrected to the standard height and neutral conditions. Comparison against 10-metre winds uncorrected for neutral stability can introduce biases of around 0.2 m s^{-1} (Mears et al. 2001; Chelton and Freilich 2005). U_{10N} is calculated by extrapolating the observed wind up to a standard 10 m height and correcting for the atmospheric stability. This requires estimates of the heat and momentum flux (e.g. Liu and Tang 1996) that are only available from a sub-set of the OceanSITES network measuring all the necessary observations (wind, air temperature, humidity and pressure, sea surface temperature, precipitation, long- and short-wave radiation).

The set of validation sites consists of 14 OceanSITES moorings collecting all the required observations during the validation period. The Global Tropical Moored Buoy Array (McPhaden et al. 2010) operated by the U. S. National Data Buoy Centre (NDBC) contributes just over half of the buoys: four sited on the equator in the Pacific Ocean from the Tropical Atmosphere Ocean (TAO) array (McPhaden et al. 1998), three from the Prediction and Research Moored Array in the Tropical Atlantic (PIRATA; Servain et al. 1998) and one in the Bay of Bengal from the Research Moored Array for African-Asian-Australian Monsoon Analysis and Prediction (RAMA, McPhaden et al., 2009). The Woods Hole Oceanographic Institution (WHOI) contributes three buoys: the Stratus Deck Region of the Eastern Pacific (STRATUS, see Raymond et al. 2004), the north- west tropical Atlantic (NTAS), and the central Pacific WHOI Hawaii Ocean Time- series Site (WHOTS). The Pacific Marine Environmental Laboratory (PMEL), the Japan Agency for Marine-Earth Science and Technology (JAMSTEC), and the Australian Bureau of Meteorology contribute one buoy each: Station Papa in the northeast Pacific (Kamphaus et al. 2008), the Japanese Kuroshio Extension Observatory (JKEO, see: Cronin eta l. 2008; Konda et al. 2010) and the Integrated Marine Observing System (IMOS: see Meyers 2008; Hill 2010) SOFS mooring (Schulz et al.) in the Southern Ocean. The three WHOI and one Australian Bureau of Meteorology buoys do not contribute to the Global Telecommunications System (GTS) and are not available for real-time calibration of Ocenasat-2, therefore providing a more robust independent validation.

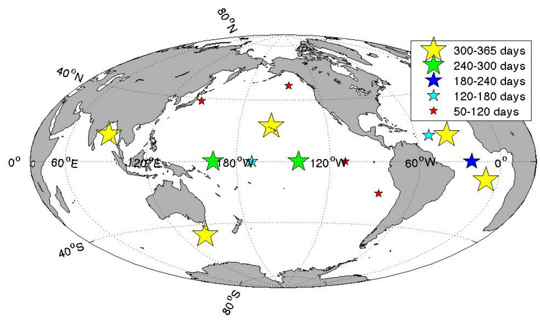

Figure 1: *OceanSITES moorings used in the 17 March 2010 to 17 March 2011 validation. The colour and size of the marker represents the number of day observations available at each site for the validation.*

Wind observations from the buoys are treated as the "ground truth" in this study, but they do contain uncertainties due to instrument accuracy and sampling conditions. Most buoys use the RM Young prop vane anemometer (model 05103) which has an accuracy of ±0.3 m s^{-1} (or 3%) and 5°-7.8° (e.g. Cronin et al., 2006). Some buoys such as SOFS, use sonic anemometers which have slightly better accuracies of around 2% in speed and ±2° in direction. The observational uncertainty was estimated at the JKEO mooring by Tomita et al. (2010) as ±0.135 m s^{-1}. Colbo and Weller (2009) estimate a maximum daily averaged uncertainty of 0.1 m s^{-1} (or 1%), while Schulz et al. (2012) found hourly buoy-ship observation differences of around 1 m s^{-1} at SOFS under moderate to strong wind speeds.

The locations and number of days of data available during the validation are displayed in Figure 1. In total there was 3100 data days available. The network is sparse and biased towards the tropical and northern hemisphere, with only one mooring in the Indian Ocean (Bay of Bengal) and one south of the Tropic of Capricorn in the Southern Ocean. Many of the buoy datasets are missing large sections of the validation period due to instrument failure, with some providing only a few months of data

Oceansat-2 Scatterometer

Oceansat-2 performs a polar sun synchronous orbit at an altitude of 720 km. The inclination is 98.28° with a local equator crossing time of around 12:00 noon. A repeat cycle is achieved every two days and planned mission life is 5 years. The swath width is 1800 km with a spatial resolution of 50 km, covering 90% of the ocean surface in 24 hours. The Ku band is sensitive to precipitation and cloud and while reliable returns are not available under such conditions (e.g. Draper and Long, 2004), quality control flagging is effective (O&SI 2012).

Oceansat-2 carries a conically scanning pencil-beam scatterometer with two beams projecting approximately 25 km × 55 km footprints on the ground (Figure 2), Padia (2010). The outer vertical polarisation beam (VV, incident angle 49°) and inner horizontal polarisation beam (HH, incident angle 43°) sweep the surface in a circular pattern. As the satellite progresses along its track, each patch of ocean is viewed four times (two beams, once looking forward, and once back) in the region covered by both the inner and outer beams. At the outer swath, greater than 700km from the centre cell, Wind Vector Cells (VWC) are only covered by VV-polarised outer beam data (O&SI 2012) generating ambiguous solutions and noisy results. In the central 'nadir' part of the swath the difference between the forward and backward azimuth view angle approaches 180° which yields noisy results (the optimal is 90°).

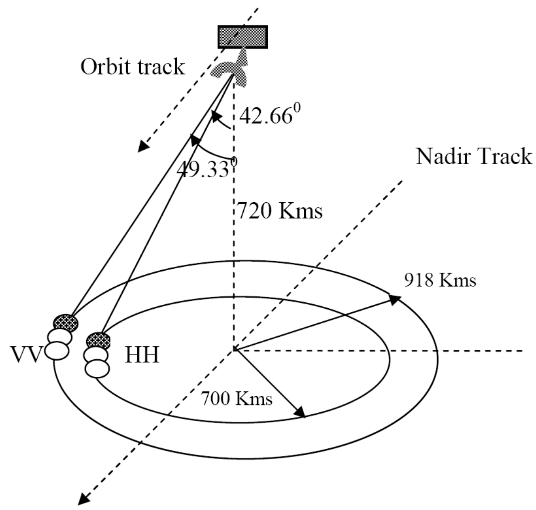

***Figure 2**: Scatterometer geometry for Oceansat-2. From Padia (2010).*

Oceansat-2 data is provided as a number of products. Here we are interested in the Level-2b data (wind vectors along the swath) in HDF5 format (Padia, 2010). The Level-2b data sets provide wind vector information and a set of quality flags used to identify the surface over which the observation is made, the presence of rain, issues with input data and issues with the retrieval process. Additionally, the files hold a selection array used to select the solution with the greatest probability. The estimation of a wind vector from a scatterometer observation is an ill-posed problem, dependent on the view geometry of multiple looks at the ocean to determine the wind. As such, multiple solutions are found. However, each of these solutions may be assigned a probability. For each retrieved wind vector a selection array, holding the index of the most likely solution, is provided. The data has been created using ISRO processor version 1.2 (Attribute "Processor Version" in the HDF5 data files).

Method and Results

The mooring data was downloaded in OceanSITES NetCDF format from (www.oceansites.org/data) for the validation period. The data was visually inspected and any suspect data rejected. Missing or suspect air pressure and precipitation were given constant values of 1013 hPa and 0 mm hr^{-1} respectively as they play only a minor role in computing the heat and momentum fluxes. All observations were averaged to a daily value, assigned a 1200 UTC time stamp, and then input to the COARE bulk flux algorithm version 3 (Fairall et al. 2003) to compute U_{10N}. The varying heights of sensors for each location were included in the calculations. Ocean surface velocity observations were not available for all moorings so were excluded from all calculations. Omitting ocean currents is expected to introduce uncertainty in the wind speed comparison that will only be significant for locations with strong ocean surface currents such as the Kuroshio (JKEO). The warm-layer diurnal variability option was not used in the code as only a single daily calculation was performed. The cool skin option was used.

Oceansat-2 Level-2b data in HDF5 format was automatically retrieved from the ISRO Oceansat-2 web server. Oceansat-2 wind ambiguities were extracted in a grid centred on mooring positions for the duration of the validation period. Ambiguity selection is based on the WVC selection and quality flag (WVC_quality_flag). The first WVC was selected for each data point, and accepted if the WVC quality flag was equal to 1. The closest accepted data around the mooring position was then linearly interpolated to the mooring location. The distance between each observation and the centre of the swath and the direction of the orbit were included, as these have been shown to be significant classifiers in past studies (e.g Chelton and Freilich 2005).

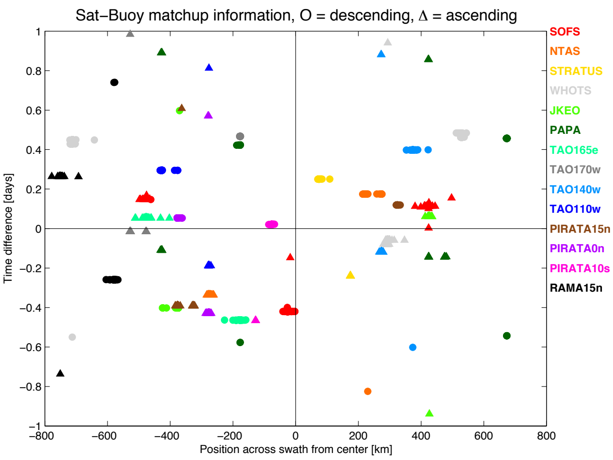

Figure 3: *Oceansat-2 – buoy match-up information for 17 March 2010 – 17 March 2011: Buoy name (colour), orbit direction (descending (o) or ascending (Δ), position along swath (positive is to the right of the centre), and time difference between day-averaged buoy and instantaneous satellite observations. Positive values indicate satellite time is before buoy time (midday UTC).*

Satellite-buoy match-ups were obtained by selecting at most one value falling within the temporal window of the daily average and closes to noon UTC, and a buoy location within 800 km of the swath centre. The 14 buoys yielded 1975 matchups over the 1-year validation period from ascending and descending orbits at a range of swath distances and time differences (within the ±12-hour window). Figure 3 displays the swath position and time difference for each matchup stratified by buoy location and orbit direction. Each location has a characteristic distribution depending on the number of possible satellite swath overpasses in a day. For example, SOFS matchups (located at 46.74S 142E) are characterised by direct descending overpasses at around 0800 local time, 10 hours after the buoy day-average observing time 2200 local (1200 UTC) and ascending passes approximately 1900 local time, three hours before the buoy day-average observing time. The ascending passes are split between the right hand and left hand sides of the swath in the 400-500 km range. Another example is the TAO165E buoy (located on the equator at 165E) that is characterised by ascending passes 400-600 km to the left of the swath centre at around 2200 (1 hour before the buoy day-average observing time), and descending passes 160-200 km also to the left of the swath centre at around 1200 local time (11 hours before the day average time).

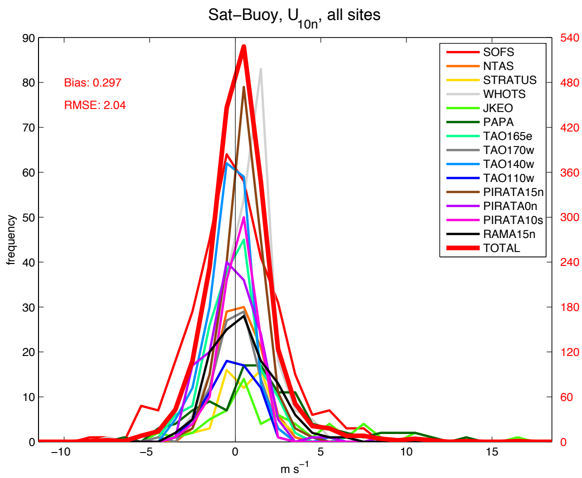

Figure 4: *Histogram of the satellite scatterometer minus in situ buoy match-up observations. The overall result is depicted by the thick red line (right y-axis). Results for individual locations are plotted in various colours with thin lines (left y-axis).*

Oceansat-2 observations of U_{10N} wind speed, direction and associated vectors were verified. Figure 4 displays a histogram of the satellite scatterometer minus in situ buoy U_{10N} match-up observations. The overall result is depicted by the thick red line (right *y*-axis), while individual locations are plotted in various colours with thin lines (left *y*-axis). Oceansat-2 overestimates U_{10N} by 0.3 m s^{-1} with a root-mean-square difference of 2 m s^{-1} based on 1975 matchups. The mean and standard deviation of satellite minus buoy matchups, grouped according to buoy and orbit, are displayed versus absolute distance from swath centre (Figure 5) and time difference (Figure 6). The ascending orbits have larger (more positive) bias compared to descending orbits for 12 out of 14 buoy sites. For absolute bias ascending orbits are larger for 11 out of 14 sites.

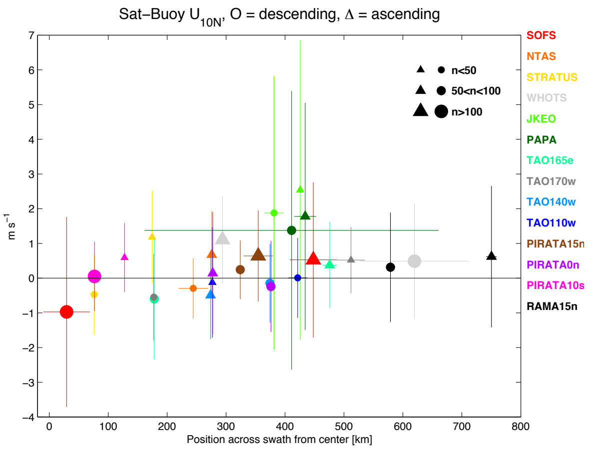

Figure 5: *U_{10N} mean and standard deviation differences between Oceansat-2 and buoys displayed as a function of location (colour), orbit direction (descending (o) or ascending (Δ)) and absolute position across swath for 17 March 2010 – 17 March 2011.*

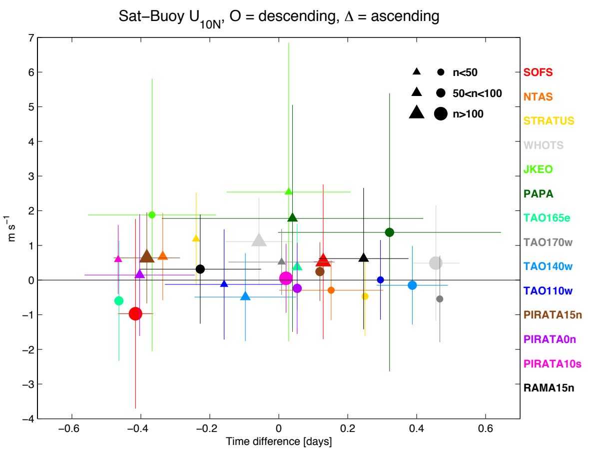

Figure 6: *The same as for figure 4 except absolute position across the swath has been replaced with time difference between day-averaged buoy and instantaneous satellite observations (positive values indicate satellite time is before buoy time (midday UTC)). The standard deviation is represented by thin lines. The number of observations in each statistic is indicated by the symbol size. The difference is calculated as Oceansat-2 minus buoy and a positive value indicates Oceansat-2 values are larger than the buoy value.*

Grouping matchups from all buoy sites together allows some trends in satellite-buoy U_{10N} statistics to be determined. The U_{10N} bias for descending orbits is symmetrical around the swath centre, underestimating in the swath centre by around -0.5 m s^{-1} and overestimating by around 0.25 m s^{-1} beyond about 300 km (Figure 7). The ascending orbit is also symmetrical around the swath centre, ignoring smaller sample size statistics, but the bias is always positive at around 0.5 m s^{-1}. Matchups in particular swath ranges may be dominated by just a few buoy locations and satellite-buoy time lags. For example, the swath range -800 km to -600 km is dominated by matchups from RAMA15N and WHOTS (descending orbit), while the central region ±100 km is dominated by SOTS and PIRATA10S (descending orbit). Therefore matchup biases may be a function of swath position and time lag. Bias binned as a function of satellite-buoy time difference (Figure 8) does not provide any further insight.

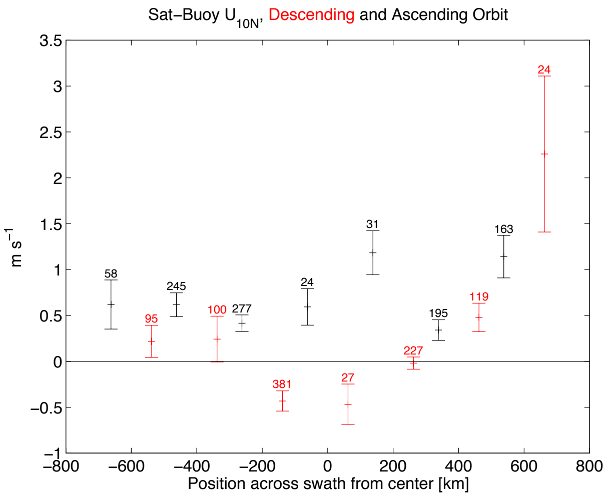

Figure 7: *Satellite-Buoy U_{10N} matchup statistics (mean, standard error of the mean and sample size), binned in 200 km increments according to position from swath centre for descending (red) and ascending (black) orbits. Sample sizes less than 10 are not displayed.*

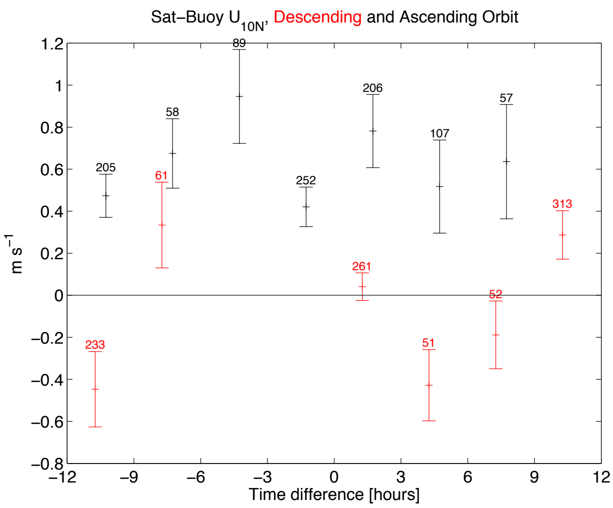

Figure 8: *Same as for figure 6 except binned in 3-hour increments of satellite-buoy time. Positive values indicate satellite time is before buoy time (midday UTC).*

Bias is also displayed as a function of the in situ buoy wind speed U_{10N} (Figure 9), and there is some indication of a positive bias at the lowest wind speed (0-2 m s^{-1}) and also for ascending orbits at all wind speeds with the smallest bias in the 4-6 m s^{-1} buoy wind range. A combined analysis of bias as a function of swath position and buoy wind speed

(Figure 10) yields only limited further insight, probably due to the small sample size. Overall, bias increases with wind speed, although the 350-700 km positive swath yields the lowest bias in the 5-10 m s-1 wind speed range.

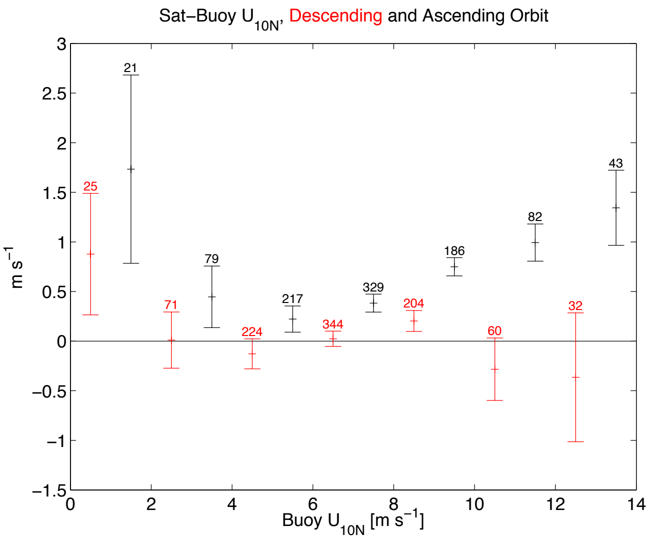

Figure 9: *Same as for figure 6 except binned in 2 m s-1 Buoy U10N wind speeds.*

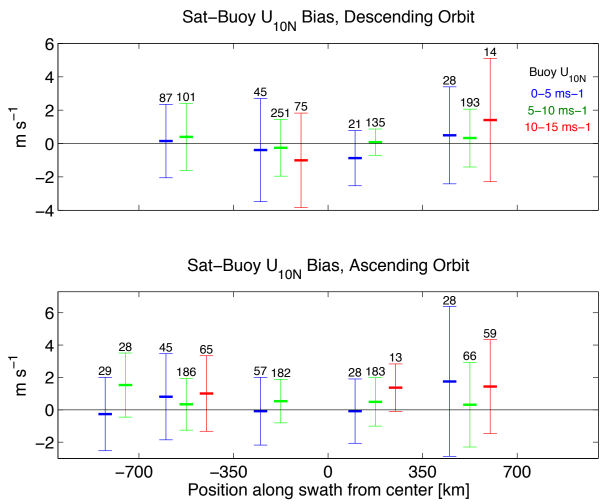

Figure 10: *Satellite-buoy U10N bias and RMS difference binned by swath position (with bin edges at -800, – 700, -350 km, 0, 350, 700, 800 km) and buoy wind speed U10N (5 m s-1 increments) for descending (top panel) and ascending (bottom panel) orbits. Sample size is indicated for each bar. Sample sizes less than 10 are not displayed. Note there are no matchups in the 700-800 km bin.*

The RMS difference is largest for the lowest (0-5 m s-1) and highest (10-15 m s-1) wind speed bins, but that may be due to the smaller sample sizes in those bins.

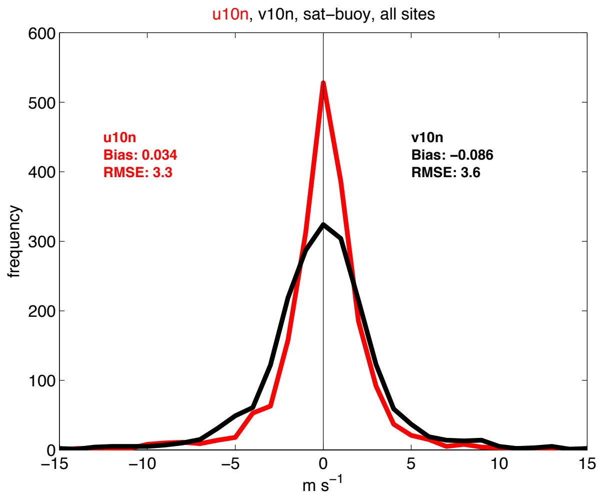

Figure 11: *Histogram of the satellite scatterometer minus in situ buoy match-up observations for wind vector components U10N (red) and V10N (black).*

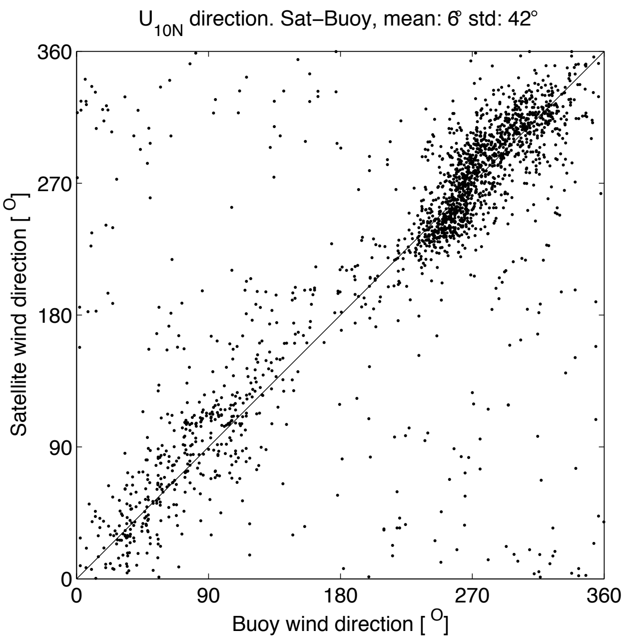

Figure 12: *Wind direction matchups for the satellite and buoys. Wind direction is in the going towards (oceanographic) convention.*

The wind vector components U_{10N} and V_{10N} are also compared (Figure 11) and show very small biases of 0.03 m s-1 and -0.09 m s-1 respectively. The root-mean-square differences are 3.3 m s-1 and 3.6 m s-1 respectively. The corresponding wind directions (going to convention) for the satellite and buoys (Figure 12) show good agreement for the most part with a mean directional difference of 6° and some spread (standard deviation 42°). There is a concentration of observations in the 225°-315° band (easterly winds) which dominate the results. Figure 13 displays the directional bias binned for position across swath and by orbit direction. While the ascending orbit exhibits a reasonably constant bias across the swath, the descending obit shows some asymmetry with positive bias for negative swath position and near-zero bias for positive swath position. Analysis of directional bias against time lags did not show any trends (not shown) while there is a minimum in directional differences of around 4° in the 6-12 m s^{-1} buoy U_{10N}, increasing to around 15° outside that range (not shown). The wind standard deviations within the bins are around 41° for moderate winds and slightly larger outside that range.

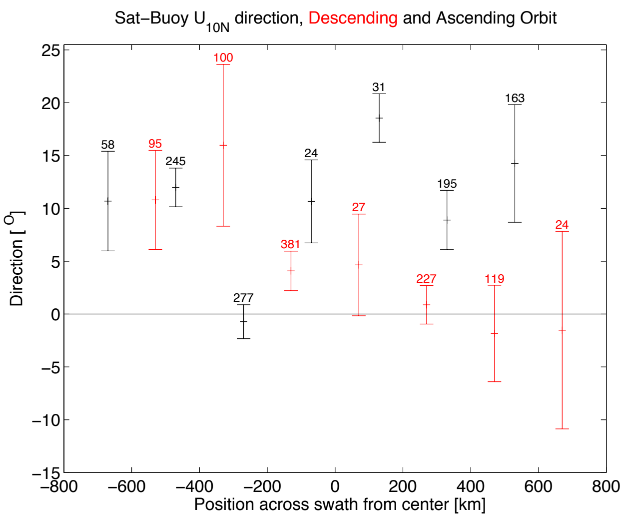

***Figure 13:** Satellite-Buoy wind direction matchup statistics (mean, standard error of the mean and sample size), binned in 200 km increments according to position from swath centre for descending (red) and ascending (black) orbits. Sample sizes less than 10 are not displayed.*

The analysis uses daily averaged in situ wind observations to allow the inclusion of timely NDBC, PMEL and JAMSTEC OceanSITES data. The impact of using higher resolution in situ data was evaluated at the SOFS site. The satellite validation was performed for daily, hourly and 1-minute buoy observations (Figure 14). Increasing the temporal resolution at the SOFS site increases the bias from -0.02 m s^{-1} to 0.07 m s^{-1} and 0.1 m s^{-1} respectively, while the RMS error is smallest at the hourly scale with corresponding values 2.5 m s^{-1}, 1.5 m s^{-1} and 1.8 m s^{-1}. The buoy mean U_{10N} during the validation period at SOFS is 10.5 m s^{-1}, giving a 1.3 hour timescale to match the 50 km satellite footprint scale. This agrees with the RMS error results described above and suggests that the ideal buoy timescale for the validation is 1-hourly, and that the daily validation presented here generates a mean satellite-buoy result that underestimates the bias and overestimates the RMS difference.

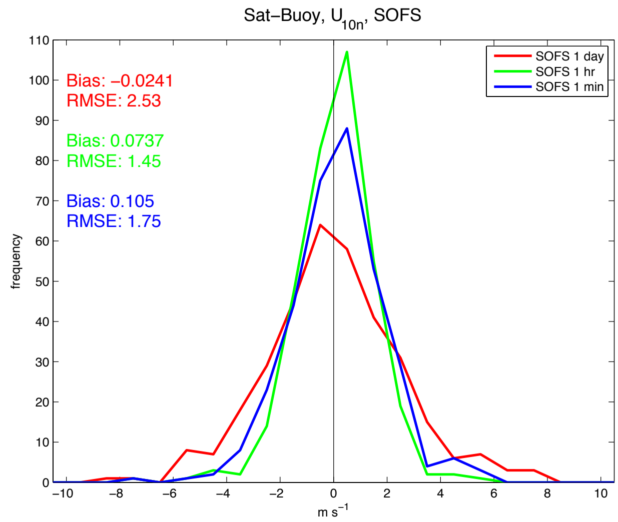

***Figure 14:** Histogram of the satellite scatterometer minus in situ SOFS buoy match-ups at 47S, 142E. for U_{10N}. Results are shown for different in situ data averaging periods: 24 hours (red, same as Figure 4), 1-hour (green) and 1-minute (blue).*

Discussion and Conclusions

Validation studies have been performed on wind products from previous satellite scatterometer missions. Chelton and Freilich (2005) compared the 9.5 month NSCAT observations and the first 2-years of QuickSCAT observations against NDBC buoy winds (with a 30 minute time window) around North America, determining biases of -0.03 m s^{-1} and 0.11 m s^{-1} respectively and RMS speed differences of 1.3 m s^{-1} and 1.2 m s^{-1}. Wind direction standard deviation differences were found to be around 14° for winds greater than 6 m s^{-1}, but increasing to 50° for calm conditions. ASCAT comparisons against buoys yield biases of less than 0.5 m s^{-1} and RMS differences less than 2 m s^{-1}. Directional biases are smaller than 2° with a standard deviation around 18°, increasing to around 26° for wind speeds less than 5 m s^{-1} (Bentamy et al. 2008).

The Oceansat-2 data stream was made available via the internet in December 2010 and there are few Oceansat-2 evaluation studies available. The EUMETSAT Ocean and Sea Ice Satellite Application Facility commenced generating Oceansat-2 scatterometer (OSCAT) level 2a and 2b wind products in July 2011 (O&SI 2012). A validation study comparing the ISRO and OSCAT products was performed (Stoffelen and Verhoef 2011) and the L2B results are briefly summarized here. Validation was performed for the period November 2009 to May 2010 against approximately 150 buoys that contribute hourly observations to the GTS, located in the tropical belt, and coastal North America and European seas. We note that these buoys do not provide sufficient observations to estimate fluxes, and calculations of U_{10N} will be less accurate than those used in this study. The standard deviation error in U_{10N} was 1.38 m s^{-1} for ISRO L2B, and 1.25 m s^{-1} for OSCAT. Direction standard deviation error was 22° and 23° respectively while std in U_{10N} and V_{10N} was 2.3 m s^{-1} and 2.2 m s^{-1} for ISRO L2B and 2.1 m s^{-1} and 2.1 m s^{-1} for OSCAT respectively.

The validation conducted here has shown that Oceansat-2 overestimates U_{10N} by 0.3 m s^{-1} with a RMS difference of 2 m s^{-1}. Wind direction comparisons show a bias of 6° and std of 42°. This is somewhat larger than the results found in other scatterometer studies. Further analysis with the SOFS buoy data suggest that changing from a daily to hourly in situ data set would alter the validation results; increasing the U_{10N} bias, and reducing the RMS difference by a factor of 0.6. If applied across the full analysis of all buoys, the result would be that Oceansat-2 overestimates U_{10N} by 1 m s^{-1} with an RMS difference of 1.2 m s^{-1}**.** The ascending orbit appears to exhibit a larger positive bias compared to the descending which may be related to the instrument geometry. There is some evidence that bias and RMS difference increases with buoy wind speed.

Acknowledgements

Acknowledgment is given to the organizations and staff that maintain the OceanSITES moorings and data-streams used in this study: NOAA (PMEL), NDBC, JAMSTEC, WHOI and IMOS. We also thank ISRO for providing the OceanSat-2 data used in the validation.

References

Atlas, R., and Coauthors, 2001: The effects of marine winds from scatterometer data on weather analysis and forecasting. *Bull. Amer. Meteor. Soc.*, **82**, 1965-1990.

A. Bentamy, A., D. Croize-Fillon, and C. Perigaud, 2008: Characterization of ASCAT measurements based on buoy and QuikSCAT wind vector observations. *Ocean Sci.*, **4**, 265–274.

Buehner, M., 2002: Assimilation of ERS-2 scatterometer winds using the Canadian 3D-var. *Atmos. Ocean*, **40**, 361–376.

Chelton, D. B., and M. H. Freilich, 2005: Scatterometer-based assessment of 10-m wind analysis from the operational ECMWF and NCEP numerical weather prediction models. *Mon. Wea. Rev.*, **133**, 409-429.

Chelton, D. B., M. G. Schlax, M. H. Freilich, and R. F. Milliff, 2004: Satellite radar measurements reveal short-scale features in the wind stress field over the World Ocean. *Science*, **303**, 978–983.

Chen, D., M. A. Cane, and S. E. Zebiak, 1999: The impact of NSCAT winds on predicting the 1997/1998 El Nino- A case study with the Lamont-Doherty Earth Observatory model, *J. Geophys. Res.*, **104**, 11321

Chen, S., 2007: The impact of assimilating SSM/I and QuikSCAT satellite winds on hurricane Isadore simulations, *Mon. Wea. Rev.*, **135**, 549-566, DOI: 10.1175/MWR3283.1

Colbo K., and R. A. Weller, 2009: Accuracy of the IMET Sensor Package in the Subtropics, *J. Atmos. Ocean. Tech.*, **26**, doi: 10.1175/2009JTECHO667.1

Cronin, M. F., Fairall C. W., McPhaden M. J., 2006: An asesemnt of buoy-derived and numerical weather prediction surface heat fluxes in the tropical Pacific, *J. Geophys. Res.*, **111**, doi: 10.1029/2005JC003324.

Cronin, M. F., C. Meinig, C. L. Sabine, H. Ichikawa, and H. Tomita, 2008: Surface mooring network in the Kuroshio Extension. *IEEE Syst. J.*, **2**, 424.

Cronin, M. F, R. A. Weller, R. S. Lampitt and U. Send, 2012: Ocean Reference Stations, Earth Observation, Rustam B. Rustamov and Saida E. Salahova (Ed.), ISBN: 978-953-307-973-8, *InTech*, Available from: http://www.intechopen.com/articles/show/title/ocean-reference-stations

Draper, D. W., and D. G. Long, 2004: Evaluating the effect of rain on SeaWinds scatterometer measurements, *J. Geophys. Res.*, **109**, C02005, doi:10.1029/2002JC001741.

Fairall, C. W., E. F. Bradley, J. E. Hare, A. A. Grachev, and J. B. Edson, 2003: Bulk Parameterization of Air–Sea Fluxes: Updates and Verification for the COARE Algorithm, *J. Clim.*, **16**, 571-591.

Figa-Saldaña, J., J.J.W. Wilson, E. Attema, R. Gelsthorpe, M.R. Drinkwater, and A. Stoffelen, 2002: The advanced scatterometer (ASCAT) on the meteorological operational (MetOp) platform: A follow on for European wind scatterometers. *Can. J. Remote Sensing*, **28**, pp. 404–412.

Fu, L-L., 2003: Wind-forced intraseasonal sea level variability of the extratropical oceans, *J. Phys. Ocean.*, **33**, 436-449.

Greenslade, D. J. M., E. W. Schulz, J. D. Kepert and G. Warren, 2005: The impact of the assimilation of scatterometer winds on surface wind and wave forecasts, *J. Atmos. Oceanic Sci.*, **10**, 261-287.

Halpern, D., M. H. Freilich, and R. A. Weller, 1998: Arabian sea surface winds and ocean transports determined from ERS-1 scatterometer, *J. Geophys. Res.*, **103**, 7799

Hill, K., 2010: The Australian Integrated Marine Observing System (IMOS). *Meteor. Technol. Int.*, **1**, 114–118.

Isaksen, L. and P. A. E. M. Janssen: 2004, Impact of ERS scatterometer winds in ECMWF's assimilation system. *Quart. J. Roy. Meteor. Soc.*, **130**, 1793–1814, doi: 10.1256/qj.03.110.

JPL, 2001: QuikSCAT science data product users' manual (version 2.2). JPL Publication D-18053, Jet Propulsion Laboratory, Pasadena, CA, 89pp

Kamphaus, R., M. Cronin, C. Sabine, S. Emerson, C. Meinig, and M. Robert, 2008: New surface mooring at Station Papa monitors climate. *PICES Press*, **16**, 26-27.

Kelly, K. A., S. Dickinson, M. J., McPhaden, and G. C. Johnson, 2001: Ocean currents evident in satellite wind data. *Geophysical Research Letters*, **28**, 2469–2472

Kent, E. C., G. B., D. I. Berry, J. Fletcher, A. Hall, S. North, S. D. Woodruff, 2009: The Voluntary Observing Ship (VOS) Scheme, in *Proceedings of OceanObs'09: Sustained Ocean Observations and Information for Society (Vol. 2),* Venice, Italy, 21-25 September 2009, Hall, J., Harrison D.E. & Stammer, D., Eds., ESA Publication WPP-306.

Kepert, J. D., D. J. M. Greenslade and G. D. Hess, 2005: Assessing and improving the marine surface winds in the Bureau of Meteorology numerical weather prediction systems. *BMRC Res. Rep.*, **105**, Bureau of Meteorology, 61 pp.

Konda, M., H. Ichikawa, H. Tomita, M. F. Cronin. 2010: Surface heat flux variations across the Kuroshio Extension as observed by surface flux buoys. *J. Clim.*, **23**, 5206-5221.

Leidner, S. M., L. Isaksen, and R. Hoffman, 2003: Impact of NSCAT winds on tropical cyclones in the ECMWF 4DVAR assimilation system. *Mon. Wea. Rev.*, **131**, 3-26

Liu, W. T., and W. Tang: 1996: Equivalent neutral wind. JPL Publication 96-17, Pasadena, CA, 8pp.

Liu, W. T., W. Tang, and H. Hu, 1998: Space borne sensors observe El Nino effects on ocean and atmosphere in North Pacific, *Eos, Trans. Amer. Geophys. Union*, **79**, 249-252.

Lorenc, A., Analysis methods for numerical weather prediction, 1986: *Q. J. Roy. Meteorol. Soc.*, **112**, 1177–1194.

Madden, R. A., T. J. Hoar, and R. F. Milliff, 2002: Scatterometer winds composted according to the phase of tropical intraseasonal oscillations, *Tellus A*, **51**, 263-272, DOI:10.1034/j.1600-0870.1999.t01-2-00007.x

McPhaden, M. J., and Coauthors, 1998: The Tropical Ocean- Global Atmosphere (TOGA) observing system: A decade of progress. *J. Geophys. Res.*, **103**, 14 169–14 240.

McPhaden, M. & Coauthors, 2010: The Global Tropical Moored Buoy Array, in *Proceedings of OceanObs'09: Sustained Ocean Observations and Information for Society (Vol. 2),* Venice, Italy, 21-25 September 2009, Hall, J., Harrison D.E. & Stammer, D., Eds., ESA Publication WPP-306.

McPhaden, M, J., G. Meyers, K. Ando, Y. Masumoto, V. S. N. Murty, M. Ravichandran, F. Syamsudin, J. Vialard, L. Yu, W. Yu, 2009: RAMA: the Research Moored Array for African–Asian–Australian Monsoon Analysis and Prediction. *Bull. Amer. Meteor. Soc.*, **90**, 459-480

Mears, C. A., D. K. Smith, and F. J. Wentz, 2001: Comparison of Special Sensor Microwave Imager and buoy-measured wind speeds from 1987 to 1997. *J. Geophys. Res.*, **106**, 11 719–11 729.

Meldrum, D., E. Charpentier, M. Fedak, B. Lee, R. Lumpkin, P. Niiler and H. Viola, 2009: Data Buoy Observations: The *Status Quo* And Anticipated Developments Over The Next Decade, in *Proceedings of OceanObs'09: Sustained Ocean Observations and Information for Society (Vol. 2),* Venice, Italy, 21-25 September 2009, Hall, J., Harrison D.E. & Stammer, D., Eds., ESA Publication WPP-306.

Meyers, G., 2008: The Australian Integrated Marine Observing System. *J. Ocean Technol.*, **3**, 80–81.

NMOC, 2006: Operational Upgrade of GASP, *Operations Bulletin*, **62**.

NMOC, 2010: Operational implementation of the ACCESS Numerical Weather Prediction systems, *Operations Bulletin*, **83**.

O&SI, 2012: SAF Oceansat-2 Wind Product User Manual version 1.1 June 2012

Padia, K., 2010: Oceansat-2 Scatterometer algorithms for sigma-0, processing and products format, Version 1.1, April 2010, Space Applications Centre.

Rao, M.V., 2010: Oceansat-2 Mission & Applications. *Bulletin of the National Natural Resources Management System*, **34**, 1-6. http://www.isro.org/newsletters/contents/nnrms/NNRMS2010.pdf

Raymond, D. J., S. K. Esbensen, M. Gregg, and C. S. Bretherton, 2004: EPIC2001 and the coupled ocean–atmosphere system of the tropical east Pacific. *Bull. Amer. Meteor. Soc.*, **85**, 1341– 1354.

Schulz E. W., J. D. Kepert, and D. J. M. Greenslade, 2007: An Assessment of Marine Surface Winds from the Australian Bureau of Meteorology Numerical Weather Prediction Systems, *Weather and Forecasting*, **22**, 613-636

Schulz, E. W., S. A. Josey and R. Verein, First Air-Sea Flux Mooring Measurements in the Southern Ocean, *Geophys. Res. Lett.*, doi:10.1029/2012GL052290, *in press.*

Senan, R., D. Sengupta, and B. N. Goswami, 2003: Intraseasonal monsoon jets in the equatorial Indian Ocean, *Geophys. Res. Lett*, **30**, 1750-1753, DOI: 10.1029/2003GLO17583

Send, U. & Co-Authors, 2010: "OceanSITES" in *Proceedings of OceanObs'09: Sustained Ocean Observations and Information for Society (Vol. 2),* Venice, Italy, 21-25 September 2009, Hall, J., Harrison D.E. & Stammer, D., Eds., ESA Publication WPP-306.

Servain, J., A. Busalacchi, M. J. McPhaden, A. D. Moura, G. Reverdin, M. Vianna, and S. Zebiak, 1998: A Pilot Research Moored Array in the Tropical Atlantic (PIRATA). *Bull. Amer. Meteor. Soc*., **79**, 2019–2031.

Simon, B., S. H. Rahman, and P. C. Joshi, 2006: Conditions leading to the onset of the Indian monsoon: A satellite perspective, *Meteorol. Atmos. Phys*., **93**, 201-210, DOI: 10.1007/s00703-005-0155-6

Stoffelen, A., and D. Anderson, 1997: Scatterometer Data Interpretation: Measurement Space and Inversion, *J. Atmos. Ocean. Tech.,* **14**, 1298

Stoffelen, A. C. M., and G. J. Cats, 1991: The impact of *Seasat-A* scatterometer data on high-resolution analyses and forecasts: the development of the *QE II* storm, *Mon. Wea. Rev*. **119**, 2794-2802

Stoffelen, A., and A. Verhoef, 2011: Validation of Oceansat-2 scatterometer data, 2011 EUMETSAT Meteorological Satellite Conference, 5-9 September 2011, Oslo, Norway

Tomita, H. M. Kubota, M. F. Cromnin, S. Iwasaki, M. Konda, and H. Ichikawa, 2010: An assessment of surface heat fluxes from J-OFURO2 at the KEO and JKEO sites, *J. Geophys. Res*., **115**, doi: 10.1029/2009JC005545

Yuan, X., 2004: High-wind-speed evaluation in the Southern Ocean, *J. Geophys. Res*., **109**, doi: 10.1029/2003JD004179